Motion vision is tuned to maximize sensorimotor energy transfer in blowfly flight

J. Sean Humbert[1*†], Holger G. Krapp[2*†], James D. Baeder[5], Camli Badrya[8], Inés L. Dawson[3], Jiaqi V. Huang[2], Andrew Hyslop[5,7], Yong Su Jung[4], Cosima Lutkus[1], Beth Mortimer[3], Indira Nagesh[3], Clément Ruah[2], Simon M. Walker[3,6], Yingjie Yang[2], Rafał W. Żbikowski[9], Graham K. Taylor[3*†]

[1*]Department of Mechanical Engineering, University of Colorado, Boulder, 1111 Engineering Drive, Boulder, 80309-0427, CO, USA.
[2*]Department of Bioengineering, Imperial College London, South Kensington Campus, London, SW7 2AZ, UK.
[3]Department of Biology, University of Oxford, 11a Mansfield Road, Oxford, OX1 3SZ, UK.
[4]Department of Aerospace Engineering, Pusan National University, Busandaehak-ro 63 beon-gil 2, Geumjeong-gu, Busan, 46241, South Korea.
[5]Department of Aerospace Engineering, University of Maryland, 4298 Campus Drive, College Park, 20742, MD, USA.
[6]Present Address: Faculty of Biological Sciences, University of Leeds, Leeds, LS2 9JT, UK.
[7]Present Address: ESTEC, European Space Agency, Keplerlaan 1, Noordwijk, 2200 AG, Netherlands.
[8]Department of Mechanical and Aerospace Engineering, University of California, One Shields Avenue, Davis, 95616, USA.
[9]School of Aerospace, Transport and Manufacturing, Centre for Autonomous and Cyber-Physical Systems, Cranfield University, Cranfield, Bedford, MK43 0AL, UK; and Spirent Communications PLC, Origin One, 108 High Street, Crawley, West Sussex RH10 1BD, UK.

*Corresponding authors.
Emails: sean.humbert@colorado.edu; h.g.krapp@imperial.ac.uk; graham.taylor@biology.ox.ac.uk;
†These authors contributed equally to this work.

Keywords: motion vision, insect flight, matched filter, sensor placement, mechanistic interpretability, observability, controllability, balanced realization, Gramian

Abstract

Biological sensors have evolved to act as matched filters that respond preferentially to the stimuli they expect to receive during ecologically relevant tasks [1–3]. For instance, insect visual systems are tuned to detect stimuli ranging from the small-target motion of mates [4, 5] or prey [6, 7] to the polarization pattern of the sky [1, 8]. In flies, individually identified neurons called lobula plate tangential cells respond to optic flow fields matched to specific self-motions [9, 10], forming the output layer of what is presently nature's best-understood deep convolutional neural network [11–13]. But what functional principle does their tuning embed, and how does this aid motor control? Here we test the hypothesis that evolution co-tunes physics and physiology by aligning the preferred directions of an animal's sensors to the most dynamically-significant directions of its motor system [14]. We build a state-space model of blowfly flight by combining visual electrophysiology, synchrotron-based X-ray microtomography, high-speed videogrammetry, and computational fluid dynamics. We then apply control-theoretic tools to show that the tuning of the fly's widefield motion vision system maximizes the flow of energy from control inputs and disturbances to sensor outputs, rather than optimizing state estimation as is the conventional approach to sensor placement in engineering [15, 16]. We expect the same functional principle to apply across sensorimotor systems in other organisms, with implications for the design of novel control architectures for robotic systems combining high performance with low computational load and low power consumption.

Main

Like fifth-generation fighter aircraft and small multi-rotors, flying insects are inherently unstable. This makes them highly manoeuvrable, but demands exquisite control. Technological and biological systems achieve this by combining information on sensor output and motor input with an internal model of their dynamics [17] which enables them to observe and control their motion state in the face of external disturbances. But whereas modern fly-by-wire control systems have a computationally-intensive architecture involving recursive state estimation and comparatively few sensors and actuators, insects have evolved a computationally-efficient control architecture involving simple parallel processing and many sensors and actuators [14]. For example, the blowfly *Calliphora* fuses the output of $\sim 10^5$ sensory cells to provide information on its motion state and uses at least 26 steering muscles to control its wingbeat, yet it weighs a mere 10^{-4} kg and consumes only 10^{-2} W of metabolic power in flight. Its sensor-rich control architecture may therefore point to a novel flight control paradigm in which sophisticated sensing reduces computational complexity [18]. That being so, what is special about how an insect's sensory system is configured?

One hypothesis is that the sensory systems of insects are specifically tuned to detect excitation of the natural modes of motion characterising their flight dynamics [14]. This principle, which we call the "mode-sensing hypothesis" [14, 19], would mean that rather than having to make a calibrated measurement of some physical quantity such as angular velocity or airspeed, an insect's sensors need only be sensitive to certain characteristic patterns of self-motion [20]. This accords with the non-orthogonal arrangement of most biological sensors, and with the observation that biological sensors are exquisitely sensitive to change, yet poor at measuring absolutes [14]. The same mode-sensing principle might also explain why neurons relaying sensory information to the insect flight

motor fuse information from multiple sensory modalities [14]. The sensor-rich control architecture of insects could therefore offer a novel bio-informed design principle for agile flight control [18], but the control-theoretic principle that it embodies has yet to be tested [19]. Here we address this challenge by building a state-space model of blowfly flight dynamics and control, which we use to identify the functional principle according to which visual physiology is matched to flight physics.

Modelling approach. The simplest possible state-space model of insect flight [21] linearizes the six degrees of freedom of rigid-body motion (Fig. 1A) about some equilibrium flight condition to yield the linear time-invariant (LTI) system:

$$\dot{\mathbf{x}}(t) = \mathbf{A}\mathbf{x}(t) + \mathbf{B}\mathbf{u}(t) + \mathbf{G}\mathbf{d}(t) \tag{1}$$

$$\mathbf{y}(t) = \mathbf{C}\mathbf{x}(t), \tag{2}$$

where the system matrix $\mathbf{A}$ characterises the insect's natural response to perturbations in its motion state $\mathbf{x}$; where the control matrix $\mathbf{B}$ and disturbance matrix $\mathbf{G}$ characterise the insect's forced response to control inputs $\mathbf{u}$ and aerodynamic disturbances $\mathbf{d}$; and where the output matrix $\mathbf{C}$ characterises how the motion state $\mathbf{x}$ is represented directly in the insect's sensor outputs $\mathbf{y}$. Together, the state equation (Eq. 1) and the output equation (Eq. 2) describe the transfer of system energy from control inputs and disturbances to sensor outputs through the evolution of the system state.

Creating such a model is extremely challenging because of the need to parameterize the various matrices $\mathbf{A}$, $\mathbf{B}$, $\mathbf{C}$ and $\mathbf{G}$ empirically. Moreover, whilst the state vector $\mathbf{x}$ and disturbance vector $\mathbf{d}$ can be defined from first principles, the sensor outputs $\mathbf{y}$ and control inputs $\mathbf{u}$ must be defined with reference to the insect's neuronal circuits and wing kinematics. Many of the $\sim 10^5$ sensory cells that a blowfly uses in flight control are photoreceptors whose outputs are processed by a convolutional network of identified interneurons culminating in a pooling layer of $\sim 10^1$ optic-flow sensitive lobula plate tangential cells (LPTCs). We therefore focus our analysis of blowfly flight control on the output of the LPTCs encoding widefield optic flow, using electrophysiological recordings to parameterize the $\mathbf{C}$ matrix for *Calliphora* (Eq. 2). We then use synchrotron-based X-ray microtomography, high-speed videography, and computational fluid dynamics to parameterize the $\mathbf{A}$, $\mathbf{B}$, and $\mathbf{G}$ matrices (Eq. 1). Finally, we use dynamical systems and control theory to identify the functional principle that is embedded in the tuning of the fly's widefield motion vision system. We begin by elaborating the output equation (Eq. 2) characterising the transfer of energy from the system state to the sensors.

Visual physiology

Network architecture. Insects and other visually-oriented animals detect the optic flow stimuli that they experience during self-motion by correlating changes in luminance across neighbouring photoreceptors. This operation is implemented by a convolutional neural network comprising many repeated units of a simple neural circuit modeled as an elementary movement detector (EMD). In *Drosophila* (and probably other Diptera), the direction-selective EMD outputs are encoded by two populations of neurons called T4 and T5 cells [11], which respond to increments or decrements in luminance, respectively, with four sub-populations of each cell type representing the cardinal directions of local motion [12]. The fly's EMD array thereby preserves the input dimensions of its optical array in each of its eight output channels [22]. These local direction-selective EMD outputs, numbering $\sim 10^5$ in *Calliphora* with ~6,000 ommatidial elements per compound eye, are pooled by a handful of LPTCs forming the output layer of each optic lobe [23]. Any global tuning principle relating to the fly's self-motion must therefore be embedded in the synaptic weights of its LPTCs.

The LPTCs respond strongly to vertical or horizontal local motion, and are classified accordingly: *Calliphora* has ten vertical system cells {VS1–VS10} and three horizontal system cells {HSN, HSS, HSE} in each optic lobe [9, 23–25]. The VS and HS-cells arborize ipsilaterally, but some of their response fields extend across both visual hemispheres (Fig. 1I) because they are coupled to heterolateral elements called V-cells {V1, V2, Vx} and H-cells {H1, H2, Hx}, respectively, which relay output from the contralateral optic lobe [23, 25, 26]. The binocular VS and HS-cell outputs from the left and right optic lobes are finally combined with output from other sensory modalities involved in flight control by descending neurons that relay sensory information to the wing, leg, and neck motor systems [27, 28]. In summary, the VS and HS-cells form the output layer of the motion vision system as a whole, whilst the heterolateral cells form a shallow hidden layer that is critical to the function of this bilaterally symmetric deep network (Fig. 1H). We therefore use their characteristic responses to form the elements of the output vector $\mathbf{y}$ in Eq. 2.

Electrophysiological measurements. Characterization of the LPTCs' responses to local image motion reveals that their local preferred directions (Fig. 1B,C,F,I) closely match the local directions of optic flow associated with specific combinations of rotational and translational self-motion [10]. Specifically, the vertical system LPTCs signal combinations of heave translation and roll or pitch rotation [9, 24] (Fig. 1E), whilst the horizontal system LPTCs signal combinations of yaw rotation and sideslip or forward translation [25]. However, whereas the response fields of the VS and HS-cells have been extensively characterised, those of the heterolateral LPTCs are less well studied. To complete our model of the *Calliphora* motion vision system, we therefore characterised the V1, V2, and Vx response fields by making extracellular recordings of the cells' activity in response to local image motion, which we used to determine the spatial distribution of their local preferred directions and local motion sensitivity across the visual field (see Methods). These new data obtained in experiments on both sexes (Fig. 1B,C,F) complement and complete others already recorded intracellularly from the VS, HS and Hx cells [9, 24–26] and extracellularly from the V- and H-cells [25, 29, 30]. The preferred rotation axes of the V-cells (Fig. 1E) each coincide with different subsets of the VS-cells (Fig. 1D), suggesting that their couplings may be clustered (Fig. 1H).

Output equation. The LPTC response fields are measured in a head-fixed retinal coordinate system that is assumed to coincide with the stability axes used in our flight dynamics modelling (see Supplementary Information). This assumption is appropriate at the onset of the small perturbations that we model, but neglects the effects of compensatory head movements [31], which is reasonable to the extent that those are driven optokinetically [32, 33]. The optic flow experienced during translational self-motion varies inversely with distance to the visual environment, so for the purposes of computing the LPTC responses to rigid-body motion, we assume that the insect is positioned at the centre of a 2 m cube (see Methods). To parameterize the output equation (Eq. 2), we first compute the matrices of the partial derivatives of the motion flow field $\partial\dot{\mathbf{Q}}/\partial x_j$ with respect to every element $\{x_j\}$ of the state vector $\mathbf{x}$. We then take their inner products with the response fields $\{\mathbf{F}_i\}$ of each LPTC, where consecutive odd and even indices $i = 1, \ldots, 38$ correspond to the left and right cells of a pair, and use these to form the elements of the rows $\{\mathbf{c}'_i\}$ of the ipsilateral output matrix $\mathbf{C}'$ (Fig. 1G; Ext. Data Table 7). Finally, because the flight dynamics model (Eq. 1) splits into symmetric and asymmetric parts (see below), we form the rows $\{\hat{\mathbf{c}}_i\}$ of the bilateral output matrix $\mathbf{C}$ (Eq. 2) by taking the pairwise sums $\{\hat{\mathbf{c}}^+_k\}$ and differences $\{\hat{\mathbf{c}}^-_k\}$ of the responses of the $k = 1, \ldots, 19$

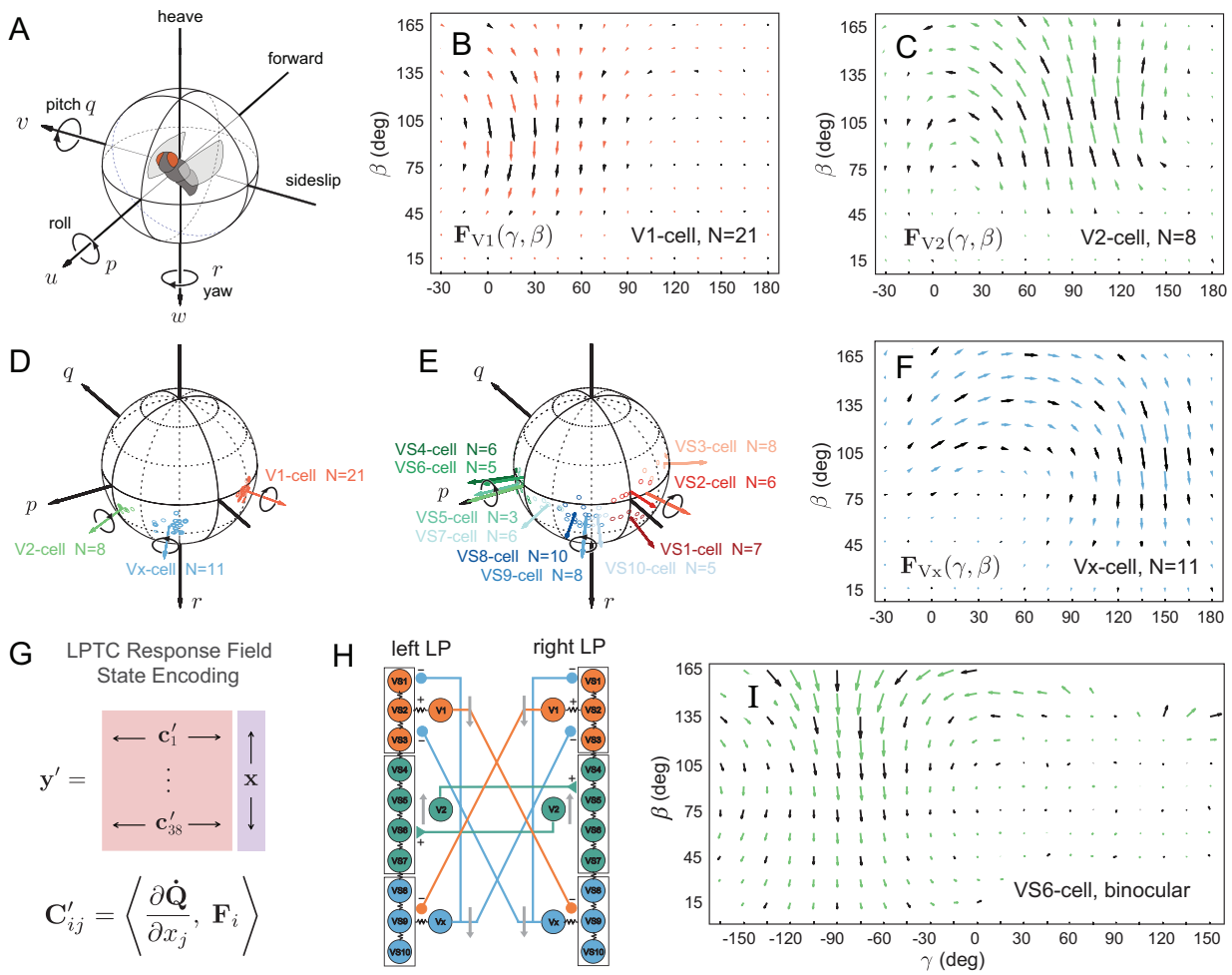

Fig. 1 Empirical parameterization of the output equation for *Calliphora*. (A) Each lobula plate tangential cell (LPTC) of the fly's motion vision system responds preferentially to some specific combination of rotational (roll, pitch, yaw) and translational (fore-aft, sideslip, heave) self-motion. (B,C,F) Measured response fields $\mathbf{F}_{V1}$, $\mathbf{F}_{V2}$, $\mathbf{F}_{Vx}$ of the right heterolateral V1, V2 and Vx cells showing their monocular response to local image motion, where N denotes the number of animals. The vector plots display the local preferred directions and local motion sensitivity of each cell in retinal coordinates of azimuth and elevation $[\gamma, \beta]$. (D,E) Preferred rotation axes of the left V1, V2, and Vx cells (new data) and left VS cells [9, 24]; the cells of the right optic lobe display mirror symmetric responses. These preferred rotation axes are computed by using an iterative least squares algorithm [34] to identify the direction of pure rotational self-motion that would maximally activate each cell given its known response field. Note that the preferred rotation axes of the V1, V2, and Vx cells are close to the mean preferred rotation axes of the VS1-3, VS4-7, and VS8-10 cells, respectively, suggesting that the VS-cells may be coupled to the heterolateral cells in functional clusters. (G) Schematic representation of the ipsilateral output equation $\mathbf{y}' = \mathbf{C}'\mathbf{x}$, where the rows $\{\mathbf{c}'_i\}$ of the ipsilateral output matrix $\mathbf{C}'$ capture the encoding of the rigid body state $\mathbf{x}$ for a given ipsilateral LPTC response field $\mathbf{F}_i$. (H) Putative coupling diagram, mapping known [35] and hypothesized connections between the VS cells and the heterolateral LPTCs V1, V2, and Vx. Colour coding signifies the proposed functional clusters. (I) Binocular response field of the left VS6-cell [26]. As the LPTCs only arborize ipsilaterally, the weak contralateral response results from coupling to the right V2 cell (C), which like VS6 responds preferentially to roll.

mirror-symmetric pairs of LPTCs and then normalizing the resulting preferred direction vectors (see Methods). This representation captures the symmetric and asymmetric components of the LPTC responses in the 38 elements of the bilateral output vector $\mathbf{y}$, thereby completing our modelling of the output equation (Eq. 2). We now elaborate the state equation (Eq. 1) describing the flow of energy from control inputs and aerodynamic disturbances to the system state.

Flight physics

Rigid-body dynamics. The insect's rigid-body flight dynamics are described by the Newton-Euler equations of motion, which relate its linear and angular acceleration to the gravitational and aerodynamic forces and moments acting on it [21]. The state vector $\mathbf{x}$ must therefore contain complete information on the insect's linear velocity $\mathbf{v} = [u\ v\ w]^T$ and angular velocity $\boldsymbol{\omega} = [p\ q\ r]^T$ with respect to an inertial reference frame (Fig. 1A). To keep the inertia tensor constant, these vector quantities are defined in body-fixed stability axes with the x-axis chosen to be aligned to the flight velocity vector at equilibrium and the y-axis normal to the insect's symmetry plane. To keep track of gravity in these rotating axes, it follows that the state vector must also contain information on the roll and pitch angles of the body $\{\phi, \theta\}$. For the LTI system in Eqs 1–2, the 8 elements of the state vector $\mathbf{x}$ are treated as small perturbations (δ) from level symmetric rectilinear flight at equilibrium, and are separated into their symmetric and asymmetric parts $\mathbf{x}_{\text{long}} = [\delta u\ \delta w\ \delta q\ \delta\theta]^T$ and $\mathbf{x}_{\text{lat}} = [\delta v\ \delta p\ \delta\phi\ \delta r]^T$, describing longitudinal and lateral motions, respectively. Wholesale movement of the surrounding air mass produces the same relative airflow as translational or rotational self-motion, so we use analogous perturbation quantities to form the aerodynamic disturbances in $\mathbf{d}$. In contrast, the control inputs in $\mathbf{u}$ must be defined empirically.

Kinematic measurements. Insect wings are passive aeroelastic structures with no discrete control surfaces, so it is challenging to identify what inputs the control vector $\mathbf{u}$ should contain. We used four high-speed video cameras to record the deforming wing kinematics of N=28 individuals over 274 flights at 3,800 fps, and used a voxel carving method [36] to identify the three-dimensional outline of the wings and estimate the pose of the body (Fig. 2H). Previous analyses have modelled insect wings as rigid flat-plates, and have treated simple summary variables such as stroke amplitude or average angle of attack as control inputs [37–39]. In reality, a blowfly's wingbeat is a coupled, three-dimensional, limit-cycle-like motion involving substantial aeroelastic deformation, driven by muscular forces applied through one of the most complex linkages in the natural world [40]. To capture this complexity, we measured the angular position of the wing tips in a body-fixed coordinate system, and estimated the torsional deformation of the wings assuming a linear twist distribution. We fitted a Fourier series with linear trend to each of the 2,708 wingbeats that we recorded for either wing, and used functional principal components analysis [41] to decompose the between-wingbeat variation in the Fourier coefficients into a set of principal components (PCs) characterising the dominant control couplings (Fig. 2G,H; see Methods). The first four PCs define an orthonormal basis for the control vector $\mathbf{u}$ that is sufficient to capture 61% of the measured variation in the Fourier coefficients. We assumed that these control inputs could be applied independently to each wing, and used them together with the wingbeat frequency f to define the nine elements of the control vector $\mathbf{u}$. Finally, we defined a set of reference wing kinematics for our aerodynamic modelling by averaging the Fourier coefficients over three wingbeats centered on the wingbeat most nearly achieving level flight among the subset of wingbeats for which the body acceleration was near-zero (< 0.5 m s^{-2}). For generality, we set the reference wingbeat frequency ($f_e = 166$ Hz), reference flight speed ($u_e = 0.85$ m s^{-1}), and reference body pitch angle ($\theta_e = 30°$) to their mean values over all the wingbeats we had measured, and used these to model a reference condition of level forward flight.

State equation. We used synchrotron-based X-ray microtomography (Fig. 2F) to estimate the inertia tensor of *Calliphora* for N=3 freshly-killed individuals, and used a Reynolds-averaged Navier-Stokes (RANS) solver (Fig. 2A,C) to model the aerodynamic forces and moments acting at the wing hinge under the reference kinematics (see Methods). Because the flight dynamics model (Eq. 1) is linearized about equilibrium, we adjusted the assumed body mass, body drag, and wing hinge moment arm so that the aerodynamic forces and moments balanced the gravitational force when integrated over the reference wingbeat kinematics. We then ran a computational experiment [42] in which we simulated the aerodynamic effect of small perturbations to the insect's motion state in $\mathbf{x}$. These perturbations are aerodynamically equivalent to the gust disturbances in $\mathbf{d}$, so having estimated the partial derivatives of the wingbeat-averaged aerodynamic forces and moments using a zero-intercept regression model (Fig. 2B), we were able to parameterize the system matrix $\mathbf{A}$ and disturbance matrix $\mathbf{G}$. We parameterized the control matrix $\mathbf{B}$ in a similar manner, simulating the aerodynamic effects of symmetric versus asymmetric control inputs (see Methods).

Each of these matrices has a block diagonal structure (Fig. 2D) reflecting the decoupling of symmetric and asymmetric motion that results from linearizing the system about a symmetric equilibrium condition. The eigenstructure of the system matrix $\mathbf{A}$ (Fig. 2E, Ext. Data Table 6) is similar to that found in other studies of insect flight dynamics [39], and is summarised here by the non-dimensional period ($\hat{T}$) and/or time constant ($\hat{\tau}$) of each mode, normalized by the insect's wingbeat period. The symmetric modes of the system are dominated by coupled pitch-heave motions, comprising a pair of fast ($\hat{\tau} = 8.4$) and slow ($\hat{\tau} = 72.9$) subsidence modes, and a slow unstable oscillatory mode ($\hat{T} = 70.0$; $\hat{\tau} = 24.6$). The asymmetric modes are dominated by coupled roll-yaw motions, comprising a slow but heavily-damped oscillatory mode ($\hat{T} = 48.1$; $\hat{\tau} = 8.2$), a fast subsidence mode ($\hat{\tau} = 2.6$), and a fast divergence mode ($\hat{\tau} = 10.7$). Hence, as the blowfly is inherently unstable in all of its axes, its sensors must therefore be used to monitor the effects of disturbances and control inputs for closed-loop flight stabilization. That being so, how has evolution tuned the visual physiology of the blowfly in relation to its flight dynamics?

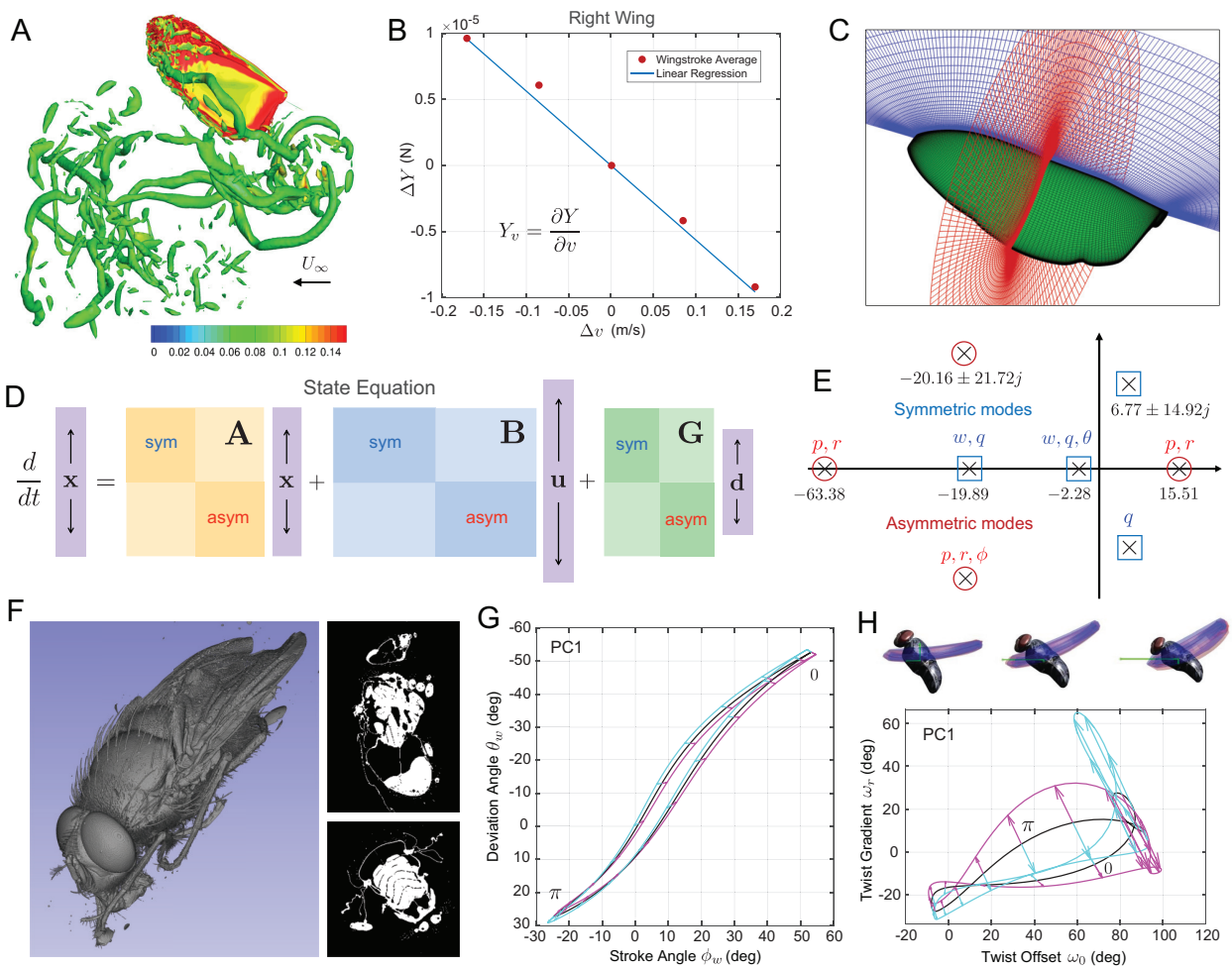

Fig. 2 Empirical parameterisation of the state equation for *Calliphora*. (A) Computational fluid dynamics (CFD) simulations for a beating wing; instantaneous wing wake structures are shown using iso-Q Criterion surfaces (0.001) and are coloured by vorticity at the end of the downstroke. Simulations capture the root and tip vortices behind the wing, and show shedding of a leading-edge vortex. (B) Zero-intercept regression of the wingbeat-averaged lateral force ΔY on the lateral perturbation velocity Δv for the right wing, shown as an example of the method used to estimate the partial derivatives of the forces and moments with respect to the rigid body motion states ($\mathbf{x}$), control inputs ($\mathbf{u}$), or aerodynamic disturbances ($\mathbf{d}$). (C) Our CFD simulations used a Reynolds-Averaged Navier-Stokes (RANS) solver utilizing an overset grid system for a body-fitted structured wing mesh and Cartesian background mesh. (D) Schematic representation of the state equation (Eq. 1) representing the blowfly's response to disequilibrium in $\mathbf{x}$, control inputs in $\mathbf{u}$, and external disturbances in $\mathbf{d}$. (E) Eigenstructure of the $\mathbf{A}$ matrix showing symmetric (i.e. longitudinal) and asymmetric (i.e. lateral) modes. (F) Synchrotron-based X-ray microtomography of a male blowfly used to estimate its inertia tensor, showing transverse and longitudinal slices and a ray-traced rendering. (G,H) Phase portraits of the first principal component (PC1) of the wing tip kinematics (stroke and deviation angle) and wing twist kinematics (twist offset and gradient), showing plus/minus one standard deviation of variation (cyan/magenta) from the mean reference wing kinematics (black). Dorsal stroke reversal occurs at phase 0, with phase π corresponding approximately to ventral stroke reversal. The inset renderings show the variation in wing and body kinematics from slow to medium to fast forward flight, where the green arrows indicate the horizontal and vertical components of mean body velocity in each flight condition.

Co-tuning of physics & physiology

Formalization of mode-sensing hypothesis. The tuning of the LPTCs is characterised by the normalized row vectors $\{\hat{\mathbf{c}}_i\}$ of the output matrix $\mathbf{C}$. Each of these rows represents a specific

direction of self-motion that the LPTCs are best-tuned to detect [19]. The mode-sensing hypothesis predicts that these preferred directions of self-motion will be matched to certain dynamically-significant directions of self-motion [14]. The dynamics of Eqs. 1–2 are summarised by a set of real symmetric matrices called Gramians, whose ordered eigenvalues $\{\lambda_j\}$ and normalized eigenvectors $\{\hat{\mathbf{v}}_j\}$ characterise dynamically-significant directions in the insect's state space. For the possibly unstable dynamical system described by Eqs. 1–2, the controllability Gramian ($\mathbf{X}_c$) and observability Gramian ($\mathbf{Y}_o$) are defined in the frequency (ω) domain [43] as:

$$\mathbf{X}_c = \frac{1}{2\pi}\int_{-\infty}^{\infty}(j\omega\mathbf{I}-\mathbf{A})^{-1}\mathbf{B}\mathbf{B}^T(-j\omega\mathbf{I}-\mathbf{A}^T)^{-1}\,d\omega \tag{3}$$

$$\mathbf{Y}_o = \frac{1}{2\pi}\int_{-\infty}^{\infty}(-j\omega\mathbf{I}-\mathbf{A}^T)^{-1}\mathbf{C}^T\mathbf{C}(j\omega\mathbf{I}-\mathbf{A})^{-1}\,d\omega, \tag{4}$$

and evaluated as solutions to a combined pair of Riccati and Lyapunov equations (see Methods). The disturbance-sensitivity Gramian ($\mathbf{X}_d$) is defined similarly to $\mathbf{X}_c$, interchanging $\mathbf{G}$ with $\mathbf{B}$ in Eq. 3.

The orthonormal eigenvectors $\{\hat{\mathbf{v}}_j\}$ of each Gramian define the principal axes of an n-dimensional ellipsoid with semi-axis lengths $\sigma_j = \sqrt{\lambda_j}$, whose longest axes correspond to the most dynamically-significant directions in the insect's state space (Fig. 3C; see Supplementary Information). For instance, the quantity $\|\mathbf{u}_{\text{opt}}\|^2 = \mathbf{x}_0{}^T\mathbf{X}_c^{-1}\mathbf{x}_0$ represents the minimum energy required to evolve the stable portion of the system to a given state $\mathbf{x}_0$ and to regulate the unstable portion of the system to the origin $\mathbf{x} = 0$. The longest axes of the controllability ellipsoid $\mathcal{E}_c = \{\mathbf{x} \in \mathbb{R}^n;\ \mathbf{x}^T\mathbf{X}_c^{-1}\mathbf{x} \leq 1\}$ thereby encode the most-controllable directions in the insect's state space (i.e., those requiring the least input energy at the controls). The observability ellipsoid ($\mathcal{E}_o$) and disturbance-sensitivity ellipsoid ($\mathcal{E}_d$) are constructed in an identical fashion, replacing $\mathbf{X}_c$ with $\mathbf{Y}_o$ or $\mathbf{X}_d$, such that $\mathcal{E}_o$ encodes the most-observable directions (i.e. those yielding the most output energy at the sensors), and $\mathcal{E}_d$ encodes the most-sensitive directions (i.e. those requiring the least disturbance energy to produce in a gust response). These three ellipsoids thereby describe the specific self-motions that the insect is best-able to drive ($\mathcal{E}_c$), best-tuned to sense ($\mathcal{E}_o$), and most-prone to experience ($\mathcal{E}_d$). Each set of dynamically-significant directions reflects a different optimization principle associated with energy flow through the system. Comparing them with the preferred directions of the LPTCs (Fig. 3) therefore allows a formal test of the mode-sensing hypothesis and the identification of any underlying optimality principle [44].

Directional tuning of LPTCs. We quantified how closely the preferred directions $\{\hat{\mathbf{c}}_i\}$ of the LPTCs were aligned to each set of dynamically-significant directions $\{\hat{\mathbf{v}}_j\}$ by taking their absolute inner products $\kappa_{ij} = |\langle\hat{\mathbf{c}}_i, \hat{\mathbf{v}}_j\rangle|$. These direction vectors represent pure symmetric or asymmetric motions, so their inner products are identically zero for symmetric-asymmetric pairings and we use κ^*_{ij} to denote symmetric-symmetric or asymmetric-asymmetric pairings, with $\kappa^*_{ij} \in [0, 1]$. The differenced responses of the three heterolateral V-cells and VS2–10 are very strongly aligned ($\kappa^*_{ij} \geq 0.9$) with the most-controllable direction of asymmetric motion, while VS1 is similarly strongly aligned with the second most-controllable direction of asymmetric motion (Fig. 3D). The summed responses of the subset {V1, Vx, VS1-2, VS8–10} are also strongly aligned ($\kappa^*_{ij} \geq 0.7$) with the most-controllable direction of symmetric motion (Fig. 3D). The same quantitative statements hold true for the disturbance-sensitivity directions, but the summed and differenced responses of the vertical system cells are only weakly aligned ($\kappa^*_{ij} \leq 0.5$) with the most-observable

directions of symmetric and asymmetric motion. In contrast, the summed responses of the HS and H-cells cells are all strongly aligned ($\kappa^*_{ij} \geq 0.7$) with the most-observable direction of symmetric motion (Fig. 3E), with the summed responses of the subset {HSE, H1, H2, Hx} being very strongly aligned ($\kappa^*_{ij} > 0.9$). Provisionally, it appears that the tuning of the vertical system cells may be related to controllability and disturbance-sensitivity, and the tuning of the horizontal system cells to observation of symmetric motions.

Overall tuning of LPTC sub-populations. To assess the overall tuning of each sub-population of LPTCs, we averaged the absolute inner products $\kappa_{ij} = |\langle \hat{\mathbf{c}}_i, \hat{\mathbf{v}}_j \rangle|$ for the $n = 10$ or $n = 3$ cells in each sub-population of LPTCs, using the semi-axis lengths $\sigma_j = \sqrt{\lambda_j}$ of the relevant ellipsoid as weights. The weighted mean alignment:

$$\eta = \frac{\sum_{i=1}^{2n} \sum_{j=1}^{8} \sigma_j \kappa_{ij}}{n \sum_{j=1}^{8} \sigma_j}, \tag{5}$$

therefore measures the overall extent to which the preferred direction vectors of a given sub-population of LPTCs encode the longest axes of a given ellipsoid. This metric generalizes to the case where the $\{\kappa_{ij}\}$ are computed by replacing the preferred directions of the LPTCs $\{\hat{\mathbf{c}}_i\}$ with a set of randomly-generated direction vectors $\{\tilde{\mathbf{r}}_i\}$ that are drawn from a uniform distribution on the unit sphere in $\mathbb{R}^8$ and then mirrored before taking their normalized sum and difference. A Monte Carlo analysis run over 100,000 sets of $n = 10$ or $n = 3$ summed and differenced directions yields an expected value of $\bar{\eta} = 0.42$ under the null hypothesis. Applying a Bonferroni correction when computing the twenty 95% confidence intervals shown in Fig. 3F, we find that the VS-cells encode the most-controllable ($\eta = 0.73$) and most-sensitive ($\eta = 0.76$) directions much more strongly than expected by chance (two-tailed $p < .0025$), but encode the most-observable directions more weakly ($\eta = 0.17$; two-tailed $p < .0025$). The V-cells display qualitatively similar properties, also encoding the most-controllable ($\eta = 0.75$) and most-sensitive ($\eta = 0.80$) directions much more strongly than expected by chance (two-tailed $p < .0025$). In contrast, the HS-cells do not encode any set of dynamically-significant directions more strongly than expected by chance ($\eta \leq 0.42$), and the H-cells actually encode the most-sensitive directions much more weakly ($\eta = 0.07$; two-tailed $p < .0025$). These results confirm that the vertical system cells are tuned to encode the effects of control inputs and gust disturbances, whereas the horizontal system cells are tuned to observe characteristics of the optic flow field that are robust to disturbances.

Joint optimization of sensing & control. The properties of controllability, observability, and disturbance-sensitivity relate to energy flow to or from the system state, and therefore depend upon our choice of coordinate system for the state vector $\mathbf{x}$. That choice is meaningful for a technological system whose internal state is represented explicitly in its programming, but is ambiguous for a biological system whose internal state cannot be directly observed. This ambiguity is eliminated by the alternative hypothesis that instead of being tuned to optimize any one such property in a given state space, the preferred directions of the LPTCs are matched to the directions of self-motion that jointly optimize controllability and observability, or disturbance-sensitivity and observability. A system that implemented this principle would be globally optimal in the sense that it would maximize the transfer of energy from input to output, and hence unique in the sense that it would not depend upon our choice of coordinate system for the state. For example, if evolution has

specifically tuned the vertical system cells to detect the effects of control inputs, then we should expect them to be strongly aligned to the joint most-controllable/observable directions. Conversely, if evolution has specifically tuned the horizontal system cells to observe characteristics of the optic flow field that are robust to gust disturbances, then we should expect them to be weakly aligned to the joint most-sensitive/observable directions.

The jointly-optimized directions of self-motion are given by the normalized column vectors $\{\hat{\mathbf{t}}_j\}$ of the transformation matrix $\mathbf{T}^{-1}$, where $\check{\mathbf{x}} = \mathbf{T}\mathbf{x}$ is a balancing transform that equalizes and simultaneously diagonalizes the transformed Gramians. Applying this balancing transform, which is unique up to multiplication by a sign matrix, we have $\check{\mathbf{X}}_c = \check{\mathbf{Y}}_o$ or $\check{\mathbf{X}}_d = \check{\mathbf{Y}}_o$, where $\check{\mathbf{Y}}_o = (\mathbf{T}^{-1})^T \mathbf{Y}_o \mathbf{T}^{-1}$ is a diagonal matrix. The diagonal entries of this matrix are the system's Hankel singular values, which may be calculated directly as $h_j = \sqrt{\lambda_j}$ where $\{\lambda_j\}$ are the ordered eigenvalues of $\mathbf{Y}_o\mathbf{X}_c$ or $\mathbf{Y}_o\mathbf{X}_d$. The Hankel singular values are similarity invariants that do not depend on the choice of coordinate system for $\mathbf{x}$, and they measure the degree of joint observability and controllability or disturbance-sensitivity in the directions $\{\hat{\mathbf{t}}_j\}$ of the original coordinate system. Importantly, although the eigenvectors of the balanced Gramians in the new coordinates are orthogonal, the directions they define in the original state space are not. To assess the overall tuning of the LPTCs to these jointly-optimized directions, we calculated their absolute inner products as $\kappa_{ij} = |\langle \hat{\mathbf{c}}_i, \hat{\mathbf{t}}_j \rangle|$, reporting their weighted mean η using the Hankel singular values $\{h_j\}$ as weights replacing the $\{\sigma_j\}$ in Eq. 5. This analysis (Fig. 3F) confirms our expectation that the VS and V-cells encode the most-controllable/observable ($\eta \geq 0.75$) and most-sensitive/observable directions ($\eta \geq 0.74$) much more strongly than expected by chance (two-tailed $p < .0025$), and that the H-cells encode the most-sensitive/observable directions much more weakly ($\eta = 0.13$; two-tailed $p < .0025$).

A functional principle of visuomotor tuning. The preceding analyses compare the randomly-generated directions $\{\tilde{\mathbf{r}}_i\}$ or preferred directions of the LPTCs $\{\hat{\mathbf{c}}_i\}$ against the biological ground truth of the parameterized state space model (Eqs. 1–2). This approach enables us to draw conclusions on the directional tuning of the individual LPTCs, but risks circularity because their preferred directions also define the output matrix $\mathbf{C}$ that is used to generate the observability Gramian $\mathbf{Y}_o$ (Eq. 4). This circularity can be avoided by composing a semi-random observability Gramian $\tilde{\mathbf{Y}}_o$ from the same system matrix $\mathbf{A}$ and a random output matrix $\tilde{\mathbf{C}}$ formed from sets of 38 randomly-generated direction vectors $\{\tilde{\mathbf{r}}_i\}$ drawn as before to respect the bilateral symmetry of the LPTCs. We then used $\tilde{\mathbf{Y}}_o$ to compute the randomized Hankel singular values as $\tilde{h}_j = \sqrt{\lambda_j}$, where the $\{\lambda_j\}$ are the ordered eigenvalues of $\tilde{\mathbf{Y}}_o\mathbf{X}_c$ or $\tilde{\mathbf{Y}}_o\mathbf{X}_d$.

Fig. 3G shows that the Hankel singular values $\{h_j\}$ associated with the fly's joint controllability/observability directions fall at the upper extreme of the null distribution of 100,000 randomly-generated sets of $\{\tilde{h}_j\}$. This confirms our conclusion that the preferred directions of the blowfly motion vision system are arranged to maximize the flow of system energy from control inputs $\mathbf{u}$ to sensor outputs $\mathbf{y}$. In fact, the first Hankel singular value provides an upper bound on system energy flow from input to output, and is higher for the biological ground truth than for any of the randomly-generated systems in Fig. 3G. Similar conclusions hold for the fly's joint disturbance-sensitivity/observability directions, and hence for the flow of system energy from gust disturbances $\mathbf{d}$ to sensor outputs $\mathbf{y}$ (Ext. Data Fig. 8B,D). Moreover, as our knowledge of how the descending neurons combine information from the LPTCs is incomplete [45–47], we verified that the same

conclusions hold when the Hankel singular values are calculated by using the mirror-symmetric responses of the LPTCs to form the 38 rows of the output matrix $\mathbf{C}'$ and mirror-symmetric pairs of randomly-generated direction vectors to form the 38 rows of the random output matrix $\tilde{\mathbf{C}}$, as opposed to their pairwise sums and differences (Ext. Data Fig. 8).

Finally, to check how the assumed nearness of the visual environment influences the fly's Hankel singular values, we synthesized 100 perturbed output matrices $\mathbf{C}$ and observability Gramians $\mathbf{Y}_o$ with respect to two different environmental configurations: a cuboid environment generated by perturbing the 2 m cube used in the analyses above, and a segmented ellipsoid environment generated by perturbing a sphere of equal nominal volume (Ext. Data Fig. 7A,C). The parameters defining each configuration were selected at random from a uniform distribution with 50% variation from their nominal values, generating variability and asymmetry in the assumed visual environment. The resulting distributions of perturbed Hankel singular values again remain at the extreme upper end of the null distribution (Ext. Data Fig. 7B,D). We robustly conclude that the directional tuning of the LPTCs embodies the functional principle of maximizing system energy transfer between the inputs and outputs of the system, as opposed to maximizing conventional design criteria such as the accuracy of state estimation.

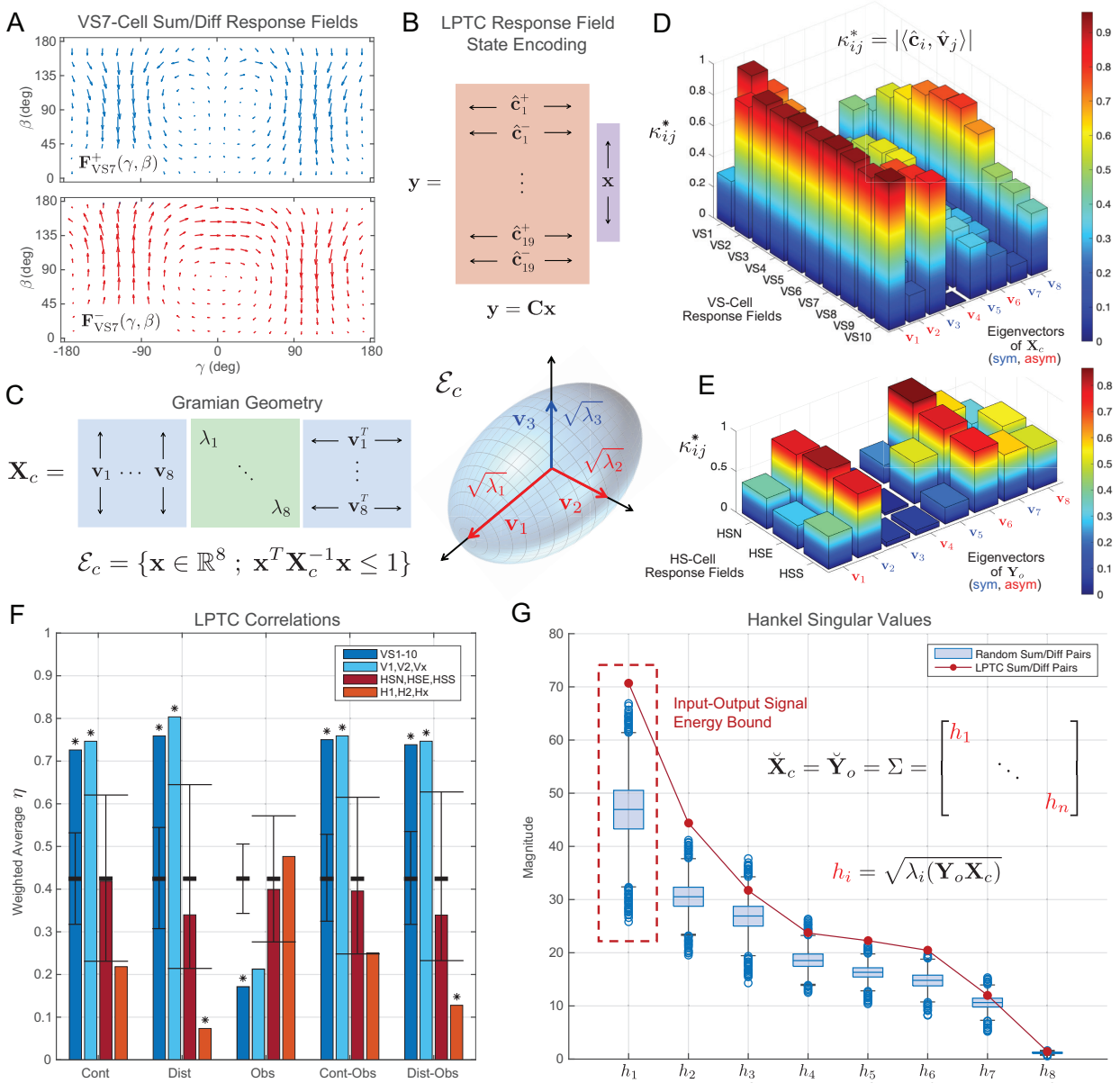

Fig. 3 Functional principles of blowfly sensorimotor design. (A) Bilaterally summed and differenced response fields for the pair of left and right VS7 cells: $\mathbf{F}^{+}_{\mathrm{VS7}}$ encodes symmetric motion; $\mathbf{F}^{-}_{\mathrm{VS7}}$ encodes asymmetric motion. (B) Schematic representation of the output equation (Eq. 2): the 38 rows of the $\mathbf{C}$ matrix contain the preferred directions of symmetric and asymmetric self-motion for the 19 pairs of LPTCs; its odd and even rows $\{\hat{\mathbf{c}}^{+}_k\}$ and $\{\hat{\mathbf{c}}^{-}_k\}$ respectively correspond to linearizations of the optic flow function $\partial\dot{\mathbf{Q}}/\partial x_j$ projected onto the bilaterally summed and differenced response fields (A) for the $k = 1, \ldots, 19$ left-right pairs of LPTCs. (C) Geometric structure of the controllability Gramian $\mathbf{X}_c$; the eigenvalues $\{\lambda_i\}$ and eigenvectors $\{\mathbf{v}_i\}$ of $\mathbf{X}_c$ form the axes and dimensions of the controllability ellipsoid $\mathcal{E}_c$. (D) Degree of alignment κ^*_{ij} between the preferred directions $\{\hat{\mathbf{c}}_i\}$ of the summed or differenced VS-cell pairs and the symmetric (blue) or asymmetric (red) eigenvectors $\{\mathbf{v}_j\}$ of the controllability Gramian $\mathbf{X}_c$. (E) Degree of alignment κ^*_{ij} between the preferred directions $\{\hat{\mathbf{c}}_i\}$ of the summed or differenced HS-cell pairs and the symmetric (blue) or asymmetric (red) eigenvectors $\{\mathbf{v}_j\}$ of the observability Gramian $\mathbf{Y}_o$. (F) Weighted mean alignment weighted by the corresponding ellipsoid axis lengths for the specified sub-populations of LPTCs. Encodings that are stronger or weaker than chance are starred ($*$). (G) The Hankel singular values $\{h_i\}$, which characterize signal energy flow through the different channels of the system, are computed for the 19 bilaterally symmetric summed and differenced pairs of normalized LPTC directions and compared to the $\{\tilde{h}_i\}$ for 100,000 sets of randomly selected 19 bilaterally symmetric summed and differenced pairs drawn from a uniform distribution in $\mathbb{R}^8$.

Discussion

How and why does the tuning of the LPTCs embed the functional principle of maximizing energy transfer between the inputs and outputs of the system? As we have shown, the vertical system LPTCs are strongly aligned to the most controllable/observable directions of self-motion (Fig. 3F). Nevertheless, the Hankel singular values are higher than would be expected by chance for all the joint controllability/observability directions (Fig. 3G). This makes sense, because the joint controllability/observability directions are non-orthogonal and with 10 pairs of VS-cells and 3 pairs of V-cells, the vertical system LPTCs have sufficient redundancy to encode all 8 directions strongly. Indeed, their mean alignment (Eq. 5) weighted by the Hankel singular values ($\eta|_{\sigma_j=h_j} = 0.75$) is only marginally stronger than their mean alignment without weighting ($\eta|_{\sigma_j=1} = 0.71$), and every one of the joint controllability/observability directions has an alignment strength $\kappa_{i,j} \geq 0.75$ with at least one VS-cell (Fig. 4A) and at least one V-cell (Fig. 4B). It follows that the vertical system LPTCs span the entire jointly observable/controllable region of the insect's state space. In contrast, the horizontal system cells encode the joint controllability/observability directions much less strongly ($\eta|_{\sigma_j=h_j} = 0.32$), in effect spanning a region of state space that is of lesser dynamical significance ($\eta|_{\sigma_j=1} = 0.30$). Similar conclusions hold for the joint disturbance-sensitivity/observability directions. Moreover, as the neck motor neurons that drive optokinetic head movements display similar response properties to the VS and HS cells [32], it is reasonable to assume that the same principle of maximizing sensorimotor energy transfer will also apply to the neck motor system.

How is this tuning principle implemented in practice? The transfer of system energy from input to output is maximized by optimizing the storage and retrieval of energy to and from the system state. For an open-loop system, energy stored in the state $\mathbf{x}$ is released through the evolution of the natural modes of the system matrix $\mathbf{A}$, which may be shaped arbitrarily through closed-loop control. Applying the principle of maximizing the Hankel singular values by tuning the sensing directions in $\mathbf{C}$ to the actuation directions of $\mathbf{B}$ through the natural modes of $\mathbf{A}$ balances the open-loop system so that it is optimized for maximum achievable closed-loop performance. The natural modes of a blowfly are dominated by pitch-heave and roll-yaw dynamics (Ext. Data Table 6), which are the same self-motions that dominate the summed and differenced responses of the vertical system LPTCs. This correspondence explains why these cells encode the jointly optimized directions so strongly (Fig. 4C–E), and makes the vertical system LPTCs particularly well-suited to modulating flight stabilization/control. In contrast, the horizontal system LPTC responses are dominated by forward motion and yaw-sideslip. With the exception of yaw, these motions are of lesser dynamical significance, but they include the equilibrium forward-flight condition about which the dynamics are linearized. It follows that the horizontal system cells are particularly well suited to encoding steady-state properties of the insect's self-motion associated with its navigational state.

The evolutionary principle that we have identified of maximizing system energy transfer from motor input to sensor output represents a radical departure from the design of current technological systems. In conventional engineering practice, optimal sensor placement is usually done at a late stage of platform design, and typically aims to maximize the accuracy of state estimation. This is achieved by maximizing the signal-to-noise ratio at the sensors, which means placing them to optimize observability [16, 48]. Tuning the LPTC response fields in this conventional manner would yield sensor outputs with the best possible signal-to-noise ratio, but if the system was rarely excited in those directions by its own actions or by disturbances, then it would not be energetically efficient to encode them. In contrast, natural selection produces neural architectures that prioritize

energetic efficiency [49], so it is reasonable to suppose that the principle of maximizing system energy throughput might also extend to the sensorimotor systems of other organisms.

As the field of robotics transitions from platforms with sensorimotor architectures composed of small numbers of discrete sensors and actuators to architectures with continuum sensing and actuation, new design principles will be required. In order to achieve optimal performance, synthesis approaches that simultaneously consider the specification of sensors, actuators, and platform dynamics will be critical. Embodied design principles that have produced nature's most effective and agile organisms, like the maximization of sensorimotor energy transfer and system energy storage/retrieval uncovered here, have the potential to revolutionize the early stage design process and maximize the performance of future engineering systems. Such bio-informed design principles will prove especially relevant in applications that—like living organisms—are resource-constrained by computational capacity and power or energy density. By analogy, our work also provides a control-theoretic framework for analysing the mechanistic interpretability of deep neural networks in cyber-physical systems.

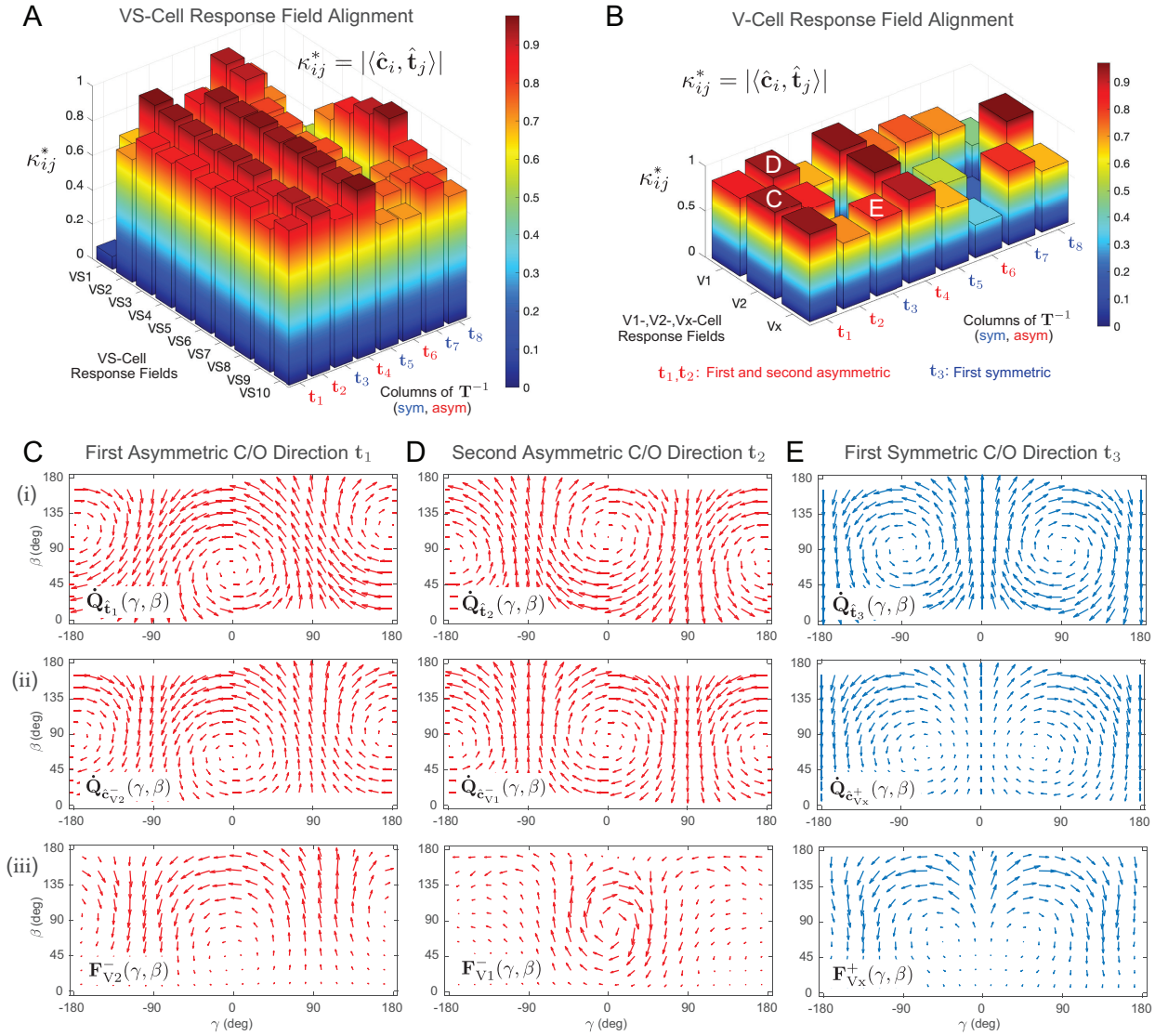

Fig. 4 Matching of the vertical system LPTCs to the fly's most-controllable/observable directions of self-motion. (A,B) Degree of alignment κ^*_{ij} between the preferred directions of self-motion of the summed or differenced VS and V-cell pairs $\{\hat{\mathbf{c}}_i\}$, and the joint controllability/observability directions of symmetric (blue) or asymmetric (red) self-motion $\{\hat{\mathbf{t}}_j\}$. The VS and V-cells are strongly aligned with the joint controllability/observability directions, and display functional similarities consistent with their coupling and clustering in Fig. 1D,E,H. (C-E) Re-projected optic flow fields $\dot{\mathbf{Q}}$ (see Methods) corresponding to: (i) the top three most controllable/observable directions $\{\hat{\mathbf{t}}_j\}$ of symmetric (blue) or asymmetric (red) self-motion (top row); and (ii) the preferred directions of symmetric (blue) or asymmetric (red) self-motion $\{\hat{\mathbf{c}}_i\}$ for each of the V-cell pairs (middle row); these are compared to: (iii) the subset of the measured summed (blue) or differenced (red) response fields $\mathbf{F}^-_{\mathrm{V2}}$, $\mathbf{F}^-_{\mathrm{V1}}$, and $\mathbf{F}^+_{\mathrm{Vx}}$, of the corresponding V-cells (bottom row). Note that the re-projected optic flow fields corresponding to the most-controllable/observable directions are even more closely matched by the re-projected optic flow fields corresponding to the preferred directions of self-motion of the V-cells than by the measured response fields of the V-cells. This difference relates principally to variation in the lengths, rather than directions, of the local motion vectors. This makes sense because the two sets of re-projected optic flow fields are reconstructed assuming that the insect is positioned at the centre of a 2 m cube (see Methods), whereas the observed variation in the local motion sensitivity of the LPTC response fields is expected to embed a nearness distribution corresponding to a natural environment [10].

Methods

Electrophysiological characterisation of LPTC response fields

Animals and dissection method. Adult male and female blowflies (*Calliphora vicina*) were taken from a laboratory colony at Imperial College London where they were kept on a 12:12 hour light:dark cycle. Flies were dissected following a standardized procedure [50]: after removing the legs, proboscis, and wings, the resulting wounds were sealed with beeswax before fixing the animal to a dedicated holder, with the thorax tilted 45° down relative to the head. The rear head capsule was opened using a micro-scalpel, and fat tissue, air sacs, and some tracheae were removed to enable placement of extracellular electrodes in the lobula plate. Saline solution [51] was added to keep the neural tissue moist. The centre of the head was positioned at the centre of a goniometric visual stimulation device, and aligned using the symmetrical deep pseudo-pupil method [52] at a precision of ±1° in head roll, pitch and yaw.

Extracellular recording and visual stimulation method. We used extracellular tungsten electrodes with 3 MΩ impedance (FHC Inc., Bowdoin, ME, USA; product code: UEWSHGSE3N1M) to record the neural activity of the V1, V2, and Vx heterolateral LPTCs. The electrodes were placed within different target areas depending on the recorded cell type using the tracheal branching patterns of the lobula plate as landmarks. Neuronal signals were amplified using a custom-built differential amplifier with a nominal gain of 10k, sampled and digitized at 20 kHz using a NI-DAQ board (USB-6211), and stored on the hard drive of a PC. Response fields were characterized only when the signal-to-noise ratio between recorded LPTC spikes and background noise was greater than 2:1, in which case a simple threshold-based method was sufficient to reliably detect time-stamped spikes of the recorded cell.

We used a custom-built automated goniometric recording platform to present a moving visual stimulus at any specified azimuth (γ) and elevation (β) in the fly's retinal coordinates. An LCD monitor (AOC AGON AG251FZ) was placed 0.3 m in front of the animal, running at a refresh rate of 240 Hz. We presented square-wave visual gratings (minimum, maximum intensity: 0.28, 265.70 cd m^{-2}; Michelson contrast: 0.9979) moving perpendicular to their orientation typically at 1 or 3 Hz temporal frequency behind a circular aperture subtending 24°. Experiments where different temporal frequencies between 0.3 - 3 Hz were applied did not affect the self-motion preferences of the cells. To assess a cell's local preferred direction (LPD) and local motion sensitivity (LMS), the grating was moved in 8 different directions at a spacing of 45°. Each motion stimulus was presented for 1 s, followed by a brief period of 0.5 s during which a homogeneous screen was presented at the mean luminance level. In total, the motion stimulus was presented at 84 positions over both eyes, covering nearly the entire 4π visual field.g

Local preferred directions and local motion sensitivities. At any given stimulus position we calculated the vector sum from the responses to the 8 different stimulus directions. Magnitude and direction of the resulting vector were taken to indicate the LMS and LPD, respectively. Those response parameters were plotted as a function of azimuth and elevation in a cylindrical projection of the fly's spherical visual field to reveal the recorded cell's global response field properties (Fig. 1B,C,F,I). Within each response field, all vectors were normalized to the maximum response measured. To facilitate recognition of the global response field organization, the measured data in Fig. 1 (black vectors) are complemented by interpolated data (coloured vectors). The data collected using this method are in line with those previously gathered using a local stimulus that changed

its motion direction continuously [32, 50, 51]. Although we presented the motion stimulus at 84 positions over both eyes, the response fields plotted for the heterolateral LPTCs in Fig. 1B,C,F show only the data obtained upon visual stimulation within the visual hemisphere that results in the highest motion sensitivity (i.e., strongest directional-selective response), which is typically the visual hemisphere ipsilateral to the dendritic input region of the recorded cell.

Modelling of LPTC response properties

Preferred self-motion parameters. We estimated each cell's preferred self-motion parameters using an iterative least squares algorithm (KvD) proposed by Koenderink and van Doorn [34]. The KvD algorithm is applied to retrieve the angular velocity $\boldsymbol{\omega}$, translational velocity $\mathbf{v}$, and the local distance distribution d of self-motion that induces an optic flow field that best fits the global response field organization of the studied cell. Hence, if we consider a given LPTC to act as a matched-filter for optic flow [10], the KvD algorithm enables us to estimate which self-motion components of a moving fly would most strongly stimulate the cell. We applied a slightly modified version of the KvD algorithm in which we assumed a homogeneous distance distribution to obtain the preferred rotation axes of the V1, V2, and Vx-cells (Fig. 1D); the preferred rotation axes of the VS-cells (Fig. 1E) were computed using a similar method by [24]. As there were no significant sex differences in the preferred rotation axes of the three heterolateral LPTCs, we pooled the response field data across sexes.

Encoding of motion state by the LPTCs. The matched filter hypothesis proposed in [10] suggests that each LPTC's output can be considered as a comparison between the cell's response field and the optic flow fields generated during the animal's self-motion, where each cell is tuned to sense a specific flow field and hence some specific combination of rotational and translational self-motion. Mathematically, this comparison can be modeled as an inner product on a discrete [10, 53, 54] or continuous [55–57] spatial domain. Here we define a spatial inner product between the instantaneous pattern of optic flow $\dot{\mathbf{Q}}$ and a given tangential cell's response field $\mathbf{F}_i$ as:

$$\mathbf{y}_i = \langle \dot{\mathbf{Q}}, \mathbf{F}_i \rangle = \int_{S^2} \dot{\mathbf{Q}} \cdot \mathbf{F}_i \, d\Omega, \quad i = 1, \ldots, m,$$

where m is the number of LPTC response fields under consideration.

The optic flow pattern $\dot{\mathbf{Q}}$ is the vector field of the relative velocity of visual contrast from objects in the environment projected into the tangent space $T_{\mathbf{r}}S^2$ of the imaging surface (Fig. 5A). Its global structure depends primarily on the observer's rotational velocity $\boldsymbol{\omega}$ and translational velocity $\mathbf{v}$. The translational contribution at each viewing direction $\mathbf{r} = (\gamma, \beta)$ is inversely scaled by the distance $d(\gamma, \beta)$ from the imaging surface to the nearest object in the environment (Ext. Data Fig. 5B). Since d can be unbounded, the nearness function $\mu(\gamma, \beta) = 1/d(\gamma, \beta)$ is commonly used in the formulation. The instantaneous optic flow pattern $\dot{\mathbf{Q}}$ on a spherical imaging surface S^2 for an arbitrary distribution of objects can be expressed as [34]:

$$\dot{\mathbf{Q}} = -\boldsymbol{\omega} \times \mathbf{r} - \mu \left[\mathbf{v} - \langle \mathbf{v}, \mathbf{r} \rangle \mathbf{r} \right].$$

In order to formulate the optic flow pattern in closed form for the calculation of the spatial inner product $\langle \dot{\mathbf{Q}}, \mathbf{F}_i \rangle$, the shape of the nearness function and its dependence on the relative pose variables $\mathbf{q} = \{x, y, z, \phi_s, \theta_s, \psi_s\}$ of the animal needs to be specified. Here $\{x, y, z\}$ are the coordinates of

the vantage point with respect to the inertial frame $\mathcal{F} = \{\hat{\boldsymbol{x}}_f, \hat{\boldsymbol{y}}_f, \hat{\boldsymbol{z}}_f\}$ and $\{\psi_s, \theta_s, \phi_s\}$ are the 3-2-1 Euler angles of the stability frame $\mathcal{S}$ relative to the inertial frame $\mathcal{F}$. For the analysis here, two classes of environment structure were considered, which included an enclosed rectangular prism and a segmented ellipsoid (Ext. Data Fig. 8). For each of these cases, the nearness $\mu(\gamma, \beta, \mathbf{q})$ is a piecewise-continuous function and the methodology for their derivation can be found in [57].

Formulation of the output matrix. For a given set of response fields $\{\mathbf{F}_i\}$, the collection of LPTC outputs form a nonlinear output equation $\mathbf{y} = \mathbf{h}(\mathbf{x})$. To characterize the rigid body state information encoded by the selected set of measured response fields, each output $y_i(x)$ is linearized about the reference flight equilibrium $\bar{\mathbf{x}}$. The resulting matrix entries in the output equation $\mathbf{y} = \mathbf{C}\mathbf{x}$ (Eq. 2) are given by

$$\mathbf{C}_{ij} = \left.\frac{\partial h_i}{\partial x_j}\right|_{\bar{\mathbf{x}}} = \left.\frac{\partial \langle \dot{\mathbf{Q}}, \mathbf{F}_i \rangle}{\partial x_j}\right|_{\bar{\mathbf{x}}} = \left.\left\langle \frac{\partial \dot{\mathbf{Q}}}{\partial x_j},\ \mathbf{F}_i \right\rangle\right|_{\bar{\mathbf{x}}}.$$

In this form, each row of the associated $\mathbf{C}$ matrix represents the state information present in the signal from a specific LPTC response field: that is, the direction it encodes in state space.

To develop the output matrix for the measured set of 19 left and right LPTC cell response fields, the raw data was first converted into stability frame coordinates according to the axis definitions of Ext. Data Fig. 6A. Note that $(\gamma, \beta) = (0°, 90°)$ in Fig. 3A is the ray along the $\hat{\boldsymbol{x}}_b$ axis in Ext. Data Fig. 5B. The recorded LPD and LMS distributions within the response fields were smoothed with a 2D Gaussian filter and then approximated with up to 8th degree spherical harmonics in the azimuth and elevation directions to facilitate an accurate numerical spatial integration. For our baseline calculation, an enclosed rectangular prism environment (Ext. Data Fig. 8A) was assumed with scaling parameters $(g_N, g_S, a_E, a_W, h_D, h_U)$ all set to a distance of 1 m, and as before the reference flight condition was set to the mean forward flight speed of $u_s = 0.8509$ m s^{-1} that we had measured (see below), such that $\bar{\mathbf{x}} = [u_s\ w_s\ q_s\ \theta_s\ v_s\ p_s\ \phi_s\ r_s]^T = [0.8509\ 0\ 0\ 0\ 0\ 0\ 0\ 0]^T$ in the stability axes. The corresponding patterns of partial derivatives of the optic flow $\partial\dot{\mathbf{Q}}/\partial x_i$ were computed by systematically perturbing each of the rigid body states and taking finite differences.

The results were used to compute the inner products numerically, resulting in the estimated response field state encoding shown in Ext. Data Table 7. To perform the subsequent analysis, we extract the entries according to the rigid body state vector from the flight dynamics model formulation, $\mathbf{x} = [\delta u_s\ \delta w_s\ \delta q_s\ \delta\theta_s\ \delta v_s\ \delta p_s\ \delta\phi_s\ \delta r_s]^T$. The states $\{\delta x_s, \delta y_s, \delta z_s, \delta\psi_s\}$ typically are not included in the linearized dynamics since a homogeneous atmosphere assumption is employed. The resulting matrix $\mathbf{C}'_{ij}$ is shown in Fig. 1G, where consecutive odd and even indices $\{i = 1, \ldots, 38\}$ correspond to the left and right cells of an LPTC pair. Finally, because the flight dynamics model (Eq. 1) splits into symmetric and asymmetric parts, we form the 38 normalized rows $\hat{\mathbf{c}}_i$ of the bilateral output matrix $\mathbf{C}$ (Eq. 2) by summing or differencing the responses of the $k = 1, \ldots, 19$ mirror-symmetric pairs of LPTCs such that $\hat{\mathbf{c}}_k^+ = (\mathbf{c}'_{2k} + \mathbf{c}'_{2k-1})/\|\mathbf{c}'_{2k} + \mathbf{c}'_{2k-1}\|$ and $\hat{\mathbf{c}}_k^- = (\mathbf{c}'_{2k} - \mathbf{c}'_{2k-1})/\|\mathbf{c}'_{2k} - \mathbf{c}'_{2k-1}\|$ as shown in Fig. 3A-B.

Re-projected optic flow fields. Any given direction of self-motion will produce a specific optic flow field in a given visual environment. We re-projected the optic flow fields $\dot{\mathbf{Q}}_{\hat{\mathbf{c}}_i}(\gamma, \beta)$ and $\dot{\mathbf{Q}}_{\hat{\mathbf{t}}_i}(\gamma, \beta)$ corresponding the specific self-motion directions $\mathbf{x} = \hat{\mathbf{c}}_i$ or $\mathbf{x} = \hat{\mathbf{t}}_i$ in state space (Fig. 4C-E) by substituting the expressions of the vectors $\boldsymbol{\omega} = [p\ q\ r]^T$, $\mathbf{v} = [u\ v\ w]^T$, and $\mathbf{r} = [\cos\gamma\sin\beta\ \ \sin\gamma\sin\beta\ \ \cos\beta]^T$ in the stability frame $\mathcal{S}$, along with an analytical expression

for the nearness of the environment $\mu(\gamma, \beta, \mathbf{q})$ into the representation for $\dot{\mathbf{Q}}$ above. The resulting azimuth γ and elevation β components (Fig. 5) of $\dot{\mathbf{Q}}$ are given by

$$\begin{aligned}\dot{Q}_\gamma &= p\cos\beta\cos\gamma + q\cos\beta\sin\gamma - r\sin\beta + \mu(u\sin\gamma - v\cos\gamma)\\ \dot{Q}_\beta &= p\sin\gamma - q\cos\gamma + \mu(-u\cos\beta\cos\gamma - v\cos\beta\sin\gamma + w\sin\beta),\end{aligned}$$

as plotted in Fig. 4C-E.

Measurement and modelling of free-flight kinematics

Animals and experimental protocol. Larval *C. vicina* were reared on red meat at 20°C until pupation; the adult flies were fed on a combination of milk powder formula and mashed banana, and were flown from 2–3 days post-eclosion. Individuals were allowed to fly freely within a 1 m diameter opaque acrylic sphere with diffuse overhead lighting. The interior of the sphere was decorated with pieces of card to provide visual contrast, and an ultraviolet light was placed at the top to stimulate flight. High-speed video sequences were captured using four synchronized Photron SA3 cameras (Photron Ltd, West Wycombe, UK) with 180 mm macro lenses (Sigma Imaging Ltd, Welwyn Garden City, UK) viewing the insect through clear portholes in the upper hemisphere, recording at 3,800 fps and 768×640 pixels. Backlighting was provided by four infrared LED lights (Dragon1IR PowerStars LED, Intelligent LED Solutions, Thatcham, UK) operating at wavelengths well beyond the visible spectrum of the insect [58] (centroid wavelength: 850 nm; spectral bandwidth at 50% intensity: 30 nm full width at half maximum). Recordings were triggered as the insect passed through the centre of the sphere, capturing forward flight punctuated by fast saccadic manoeuvres. In total, we collected $N = 2,708$ wingbeats from 205 flights by 28 individual blowflies.

Wing and body kinematics. The cameras were calibrated using a nonlinear least squares bundle adjustment routine [59] in MATLAB (The Mathworks, Inc., Natick, MA), using images of a calibration grid presented in a wide range of positions and orientations. For the main analysis, we used background subtraction and automatic thresholding to segment the pixels, and used a shape-carving method to identify the set of voxels containing the wings and body [36]. We reprojected the wing voxels as a mask for tracing the outline of the wing in each frame, and used the shape-carving algorithm on this linear feature to reconstruct the leading and trailing edges in three dimensions. We used the major axis of the body voxels to define the insect's x-axis, and the line connecting the wing roots to define the insect's transverse y-axis. We constructed a right-handed body axis system in which to measure the kinematics of the right wing, and a left-handed body axis system in which to measure the kinematics of the left wing. These were measured by defining an extrinsic y-x-z rotation sequence bringing the x-axis of a set of rotating axes initially aligned with the body axes into alignment with the wing chord connecting the trailing edge to the leading edge at some given spanwise position (r). The local pitch angle of the wing (ω), is defined as the first angle in this rotation sequence, and was measured at 6 evenly-spaced spanwise stations on the interval $r \in [0.3, 0.8]$, where r is expressed as a proportion of wing length. We summarised the instantaneous spanwise variation in ω by fitting the regression model $\omega[r] = \omega_0 + \omega_r r + \epsilon[r]$, where $\epsilon[r]$ is a Gaussian error term. We call ω_0 the twist offset, and ω_r the twist gradient. The deviation angle θ_w and stroke angle ϕ_w represent the second and third angles in the extrinsic y-x-z rotation sequence, and describe the elevation and azimuth of the wingtip in a set of body axes originating at the wing root. It follows that the insect's wing kinematics are measured by estimating $\phi_w[t]$, $\theta_w[t]$, $\omega_0[t]$, $\omega_r[t]$ for the right and left wings separately at every sample time t.

Fourier series representations of wing kinematics. For each flight sequence, we fitted quintic smoothing splines modelling $\phi_w[t]$, $\theta_w[t]$, $\omega_0[t]$, and $\omega_r[t]$ for each wing as analytical functions of continuous time t. The spline tolerance that we used for each kinematic variable was chosen to preserve information up to the 3rd harmonic of wingbeat frequency for ϕ_w and θ_w, and up to the 5th harmonic for ω_0 and ω_r. We then used a piecewise linear transform to map continuous time t onto wingbeat phase $\varphi(t)$, by taking the turning point of the summed angular velocity of both wingtips in the stroke plane to define $\varphi = 0$ as the start of the downstroke. Finally, we evaluated the splines at 101 evenly-spaced phases of each wingbeat on the interval $\varphi \in [0, 2\pi]$, so that all wingbeats were directly comparable despite variability in the wingbeat period. Fitting each wingbeat separately, we used multiple regression with time-linear and time-periodic predictor variables to model the four primary kinematic variables $\phi_w[\varphi]$, $\theta_w[\varphi]$, $\omega_0[\varphi]$, and $\omega_r[\varphi]$ as de-trended Fourier series of the form:

$$h[\varphi] = K_L\big(\varphi - \pi\big) + K_0 + \sum_{k=1}^{P} \big(K_{2k-1}\cos(k\varphi) + K_{2k}\sin(k\varphi)\big) + \epsilon[\varphi], \tag{6}$$

where $\epsilon[\varphi]$ is a Gaussian error term, and where K_L and $K_0 \ldots K_{2P}$ are fitted coefficients. The time-linear coefficient K_L accounts for the fact that any actual wingbeat cycle is unlikely to begin and end in exactly the same kinematic state, and multiplies $\big(\varphi - \pi\big)$ rather than φ so that this term has zero mean over the wingbeat cycle. The Fourier coefficients $K_0 \ldots K_{2P}$ are fitted with $P = 3$ for ϕ_w and θ_w, and with $P = 5$ for ω_0 and ω_r, to capture all of the harmonic content preserved by the quintic smoothing splines.

Functional principal components analysis. Collecting the Fourier coefficients for a single wingbeat together as $\mathbf{K}^{\phi_w} = [K_0^{\phi_w} \ldots K_{2P}^{\phi_w}]$ for the stroke angle ϕ_w, and similarly for the other primary kinematic variables, we may summarise the time-periodic variation for all N wingbeat pairs in the matrix:

$$\mathbf{Z}_\mathrm{P} = \begin{bmatrix} {}_1\mathbf{K}^{\phi_w} & {}_1\mathbf{K}^{\theta_w} & {}_1\mathbf{K}^{\omega_r} & {}_1\mathbf{K}^{\omega_0} \\ \vdots & \vdots & \vdots & \vdots \\ {}_{2N}\mathbf{K}^{\phi_w} & {}_{2N}\mathbf{K}^{\theta_w} & {}_{2N}\mathbf{K}^{\omega_r} & {}_{2N}\mathbf{K}^{\omega_0} \end{bmatrix}. \tag{7}$$

We used functional principal components analysis to decompose this matrix into a new set of time-periodic basis functions characterising the key kinematic couplings involved in flight control. This was implemented by subtracting the column means from the matrix of Fourier coefficients $\mathbf{Z}_\mathrm{P}$ to yield the centered matrix $\mathbf{Z} = \mathbf{Z}_\mathrm{P} - \bar{\mathbf{Z}}_\mathrm{P}$, and computing its singular value decomposition:

$$\mathbf{Z} = \mathbf{U}\boldsymbol{\Sigma}\mathbf{V}^T, \tag{8}$$

where $\boldsymbol{\Sigma}$ is a diagonal matrix containing the singular values of $\mathbf{Z}$, which are the positive square roots of the eigenvalues of $\mathbf{Z}^T\mathbf{Z}$ arranged in descending order. The columns of $\mathbf{V}$ contain the right-singular vectors of $\mathbf{Z}$, which are the eigenvectors of $\mathbf{Z}^T\mathbf{Z}$, normalized such that $\mathbf{V}^T\mathbf{V} = \mathbf{I}$. Because $\mathbf{Z}^T\mathbf{Z}$ is a scalar multiple of the covariance matrix of $\mathbf{Z}$, the orthonormal basis $\mathbf{V}$ that its eigenvectors define is aligned with the principal directions of the kinematic variation between wingbeats. Because each row of the principal component (PC) matrix $\mathbf{V}$ corresponds to one of the Fourier coefficients, each of its columns defines a distinct time-periodic kinematic coupling, which we refer to as PC1, PC2, etc.

Aerodynamic modelling of stability and control derivatives

Computational fluid dynamics modelling. We performed three-dimensional Reynolds-averaged Navier-Stokes (RANS) simulations of the aerodynamics of the right wing of *Calliphora* using the OVERTURNS solver [60, 61]. We simulated a reference condition of level symmetric forward flight with a freestream velocity of $U_\infty = 0.8509$ m s^{-1} and a wingbeat frequency of $f = 166.188$ Hz, corresponding to the mean values measured for these variables over the 2,708 wingbeats whose kinematics we had recorded (see above). We used a mean body pitch angle $\theta_e = 30.365°$, and defined a set of reference wing kinematics by taking the mean of $\mathbf{Z}_\mathrm{P}$ over three consecutive wingbeats centered on the wingbeat most nearly achieving level flight among the subset of wingbeats for which the body acceleration was near-zero (< 0.5 m s^{-2}). We assumed a pure laminar boundary layer based on the measured mean chord length of 2.7 mm and chord Reynolds number of 1,746. We used 720 time steps per wingbeat cycle with 12 sub-iterations, which allowed us to capture the unsteady flow characteristics with reasonable computational time. Ext. Data Tables 2 and 3 summarize the simulation parameters and input setup. The dimensions of the structured wing mesh were 195 (chordwise), 201 (spanwise), and 76 (wall-normal), and the initial wall normal spacing was 1×10^{-5} mean chord. Combined with the background mesh, this gave a total of 1.12×10^7 node points.

Computational experiments. We perturbed the reference kinematics to simulate the aerodynamic effect of control inputs and small perturbations to the motion state of the body. We used the three components of translational velocity $\{u, v, w\}$ and angular velocity $\{p, q, r\}$ referred to the body axes $\mathcal{B}$ as the perturbed states, and used the wingbeat frequency f together with principal components PC1–4 of the time-periodic wingbeat kinematics as control perturbations. Among the six perturbed states variables $\{u, v, w, p, q, r\}$, the perturbation level was set at ±10% and ±20% of freestream velocity U_∞ for the three flight velocities $\{u, v, w\}$, and at ±2.5% and ±5% of wingbeat frequency f for the three angular rates $\{p, q, r\}$. Among the five control variables, we perturbed PC1–4 by ±0.5 and ±1.0 standard deviations, and perturbed the wingbeat frequency f by ±1.5% and ±3%, corresponding to ±2.5 and ±5.0 Hz respectively. We computed the three components of aerodynamic force $\{X, Y, Z\}$ and moment $\{L, M, N\}$ referred to the body axes $\mathcal{B}$ (Ext. Data Fig. 6A). The time-averaged forces and moments had already converged reasonably by the start of the 3rd wingbeat cycle, so we obtained their wingbeat-averaged values by taking the mean of the forces and moments over the 3rd and 4th wingbeat cycles of each simulation.

Aerodynamic derivatives. In order to estimate the stability and control derivatives for our linearized flight dynamics model, we first subtracted the total aerodynamic forces and moments in each perturbed condition from those obtained in the reference flight condition, then fitted a zero-intercept linear regression through the origin to estimate the corresponding partial derivative of the aerodynamic forces and moments (Fig. 2B; Ext. Data Fig. 6D-E). The resulting aerodynamic derivatives are defined for the right wing using forces and moments resolved at the right wing hinge, and were mirrored to model the aerodynamic forces and moments on the left wing under the equivalent kinematics. The results for the left and right wings were then combined to estimate the stability derivatives (Ext. Data Table 4) and control derivatives (Ext. Data Table 5) resolved at the centre of mass, in a model enforcing equilibrium under the reference wing kinematics (see Supplementary Information for details). We used the unilateral control inputs to form sets of longitudinal control inputs $\{u_0, u_1, u_2, u_3, u_4\}$ and lateral control inputs $\{u'_1, u'_2, u'_3, u'_4\}$ through symmetric or

asymmetric application, respectively, of perturbations in PC1–4 and symmetric changes in wingbeat frequency f.

Microtomographic estimation of inertia tensor

Animals and tomographic method. Two male and one female *C. vicina* from the Imperial College London colony were sealed in 0.5 mL Eppendorf tubes, having been fed and watered to satiation and then weighed. The tubes were placed individually in the TOMCAT beamline of the Swiss Light Source synchrotron facility and were irradiated at 12 keV beam energy until the flies were dead and no further motion artefacts occurred. A 100 μm thick, Ce-doped LuAG scintillator was placed at a distance of 272 mm behind the sample to convert the transmitted X-rays into visible light. The resulting image was magnified 2-fold using an Edge 5.5 Microscope, and 1501 projection images were collected at 60 ms exposure time whilst the sample was rotated through 180°. To image the entirety of each fly, it was necessary to image three overlapping volumes in this way. Phase retrieval was performed using the Paganin algorithm [62], setting the real and imaginary parts of the deviation from one of the complex refractive index of the material to 1×10^{-7} and 1×10^{-9} respectively. Tomographic reconstruction was performed using a Fourier transform-based algorithm, resulting in voxels with an isotropic spacing of 3.25 μm.

Estimation of inertia tensor. We segmented the tomograms automatically, using thresholding and morphological operations to mask voxels corresponding to the cross-section of the Eppendorf tube and any exterior voxels. The tomograms were then combined into one continuous stack across the three samples for each specimen, using unique cross-sectional features such as hairs to align the image stacks manually along their common longitudinal axis. The complete image stack was loaded into Fiji [63], and the BoneJ plugin [64] was used to calculate the mass moments of inertia about the principal axes of the specimen, assuming a uniform density of 1.1 g cm^{-3} appropriate to insect cuticle and muscle. The mass (m) estimates arrived at using this method (Ext. Data Table 1) were identical to the weights taken at the start of the experiment to within the 0.01 g readability of the balance. Because the moments of inertia about the first and second principal axes were identical to within ±1% (Ext. Data Table 1), we set $I_y = I_z$ for the purposes of the flight dynamics modelling, and set I_x equal to the moment of inertia about the third principal axis. Assuming isometry, we non-dimensionalized the moments of inertia by dividing through by $m^{5/3}$, then rescaled these using the value of m assumed in the flight dynamics model.

Data and code availability

The data and code that support the findings of this study will be made available in figshare with the identifier doi:10.6084/m9.figshare.25504879.

Acknowledgments

The authors thank Zoe Turin, Gregory Gremillion, and Jishnu Keshavan for discussions related to the dynamical systems formulation, and Alix Leroy for discussions related to our description of the network architecture. We acknowledge the Paul Scherrer Institut, Villigen, Switzerland for provision of synchrotron radiation beamtime at the TOMCAT beamline X02DA of the Swiss Light Source (SLS), and thank Christian Schlepütz for assistance with synchrotron data collection. We thank Ric Wehling, Johnny Evers, Pat Bradshaw, and Nick Rummelt for their longstanding support of this research and for many insightful conversations.

Declarations

- **Funding.** This work was sponsored by the US Air Force Research Laboratory (AFRL), the Air Force Office of Scientific Research (AFOSR), and the European Office of Aerospace Research and Development (EOARD) under AFOSR grant no. FA-9550-09-1-0075 to J.S.H.; EOARD contract no. FA8655-09-1-3083 to H.G.K; EOARD contract no. FA8655-13-1-3077 to G.K.T. and R.W.Z.; and AFOSR grant no. FA-9550-14-1-0068 to J.S.H., H.G.K., and G.K.T. This work was supported by Beamtime Grant no. 20171617 to B.M. and G.K.T. from the Paul Scherrer Institute at the Swiss Light Source, beamline TOMCAT. I.L.D. was supported by the Biotechnology and Biological Sciences Research Council, grant no. BB/M011224/1. S.M.W. and B.M. were supported by Royal Society University Research Fellowships.

- **Competing interests.** The authors declare no competing interests.

- **Materials & Correspondence.** Correspondence and requests for materials should be addressed to G.K.T., J.S.H., and H.G.K.

- **Authors contributions.** J.S.H., H.G.K, and G.K.T. conceived the presented idea with R.W.Z. H.G.K conceived and supervised the electrophysiological experiments: J.V.H. developed the electrophysiology setup, C.R. and Y.Y, carried out the recordings, and analysed the electrophysiological data. G.K.T. and S.M.W. conceived and supervised the wing kinematic measurements: I.L.D. and S.M.W. carried out the videogrammetric experiments and analysis, and I.N. and G.K.T. carried out the functional principal components analysis. G.K.T. conducted the synchrotron experiments with B.M. and analysed the tomographic data. J.B. supervised the CFD simulations: C.B., Y.S.J, and C.S. created and performed the simulations, and J.S.H., Y.S.J, and G.K.T carried out the data analysis. J.S.H. and G.K.T. developed the theoretical framework: J.S.H., A.H., and G.K.T. conceived and performed the dynamical systems analysis. J.S.H. and G.K.T. wrote the manuscript with H.G.K. All authors participated in reviewing the manuscript.

- **Access statement.** For the purpose of open access, the authors have applied a creative commons attribution (CC BY) licence to any author accepted manuscript version arising.

Extended data figures and tables

Figures

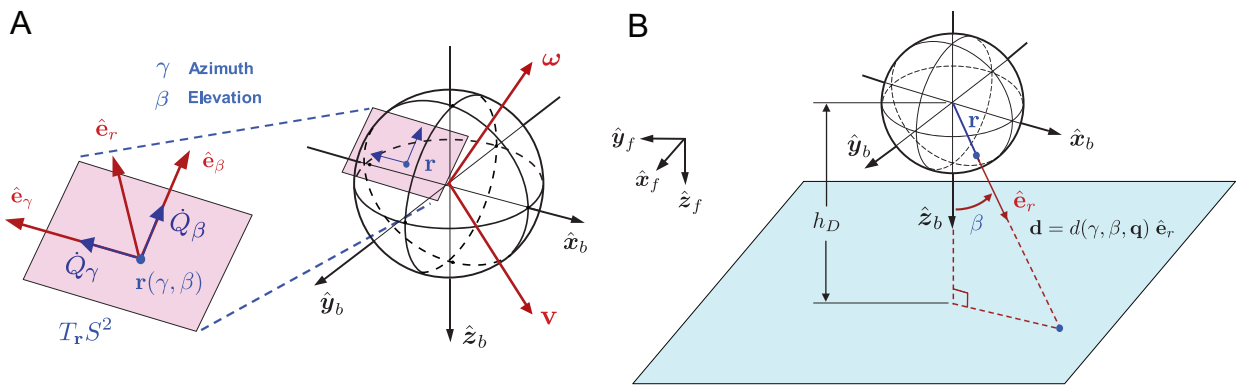

Fig. 5 Geometry for spherical optic flow. (A) The azimuth $\dot{Q}_\gamma$ and elevation $\dot{Q}_\beta$ components of the optic flow vector are the projected relative velocities $\boldsymbol{\omega}$ and $\mathbf{v}$ of visual contrasts or objects in the environment into the tangent space $T_{\mathbf{r}}S^2$ of the imaging surface, modelled here as a sphere approximating the nearly 4π visual field of the compound eyes. (B) The function $d(\gamma,\beta,\mathbf{q})$ is the distance from the imaging surface ($\mathbf{r}$) to the nearest point in the environment.

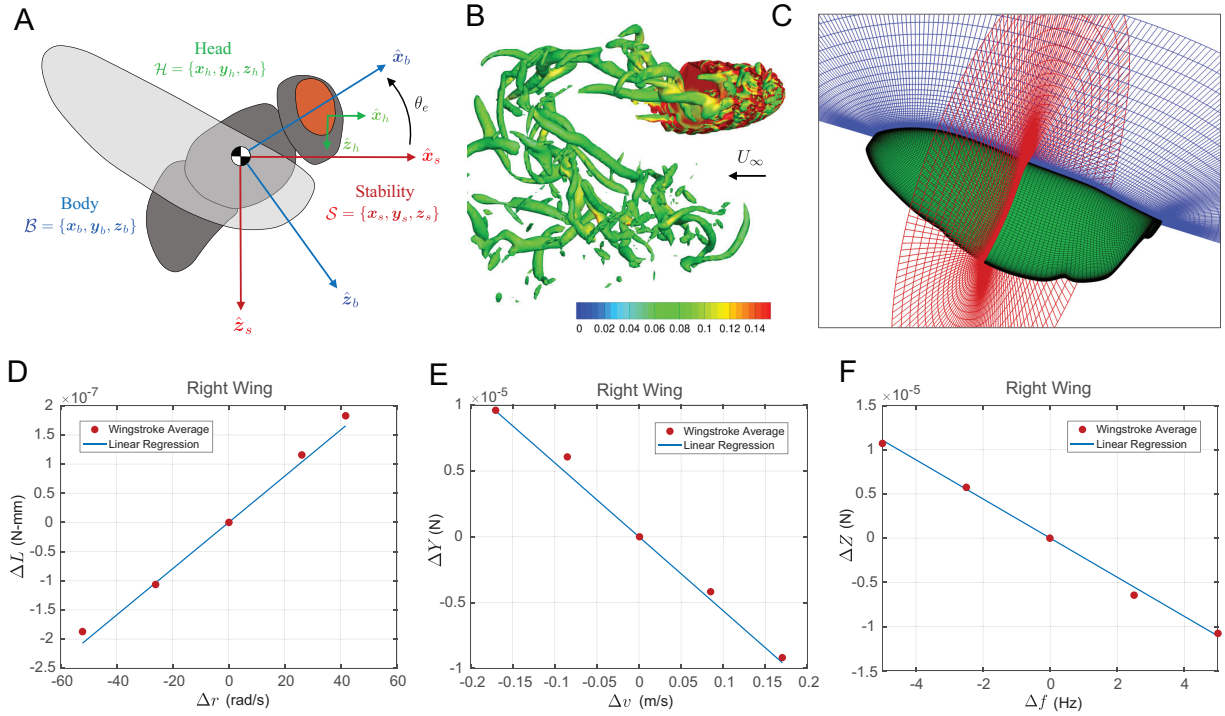

Fig. 6 Reynolds Averaged Navier-Stokes (RANS) simulations for *Calliphora* wing motions. (A) Coordinate systems for analysis include the head (visual) axes $\mathcal{H} = \{\hat{\boldsymbol{x}}_h, \hat{\boldsymbol{y}}_h, \hat{\boldsymbol{z}}_h\}$, the body (principal) axes $\mathcal{B} = \{\hat{\boldsymbol{x}}_b, \hat{\boldsymbol{y}}_b, \hat{\boldsymbol{z}}_b\}$, and the stability axes $\mathcal{S} = \{\hat{\boldsymbol{x}}_s, \hat{\boldsymbol{y}}_s, \hat{\boldsymbol{z}}_s\}$. (B) Instantaneous wing wake structures are shown using iso-Q Criterion surfaces (0.001) and colored by vorticity at the end of the upstroke. (C) Simulations utilized an overset grid system for a body-fitted structured wing mesh and a Cartesian background mesh. (D-E) Example regressed wingstroke averaged aerodynamic moments and forces as a function of perturbation states and inputs for the right wing.

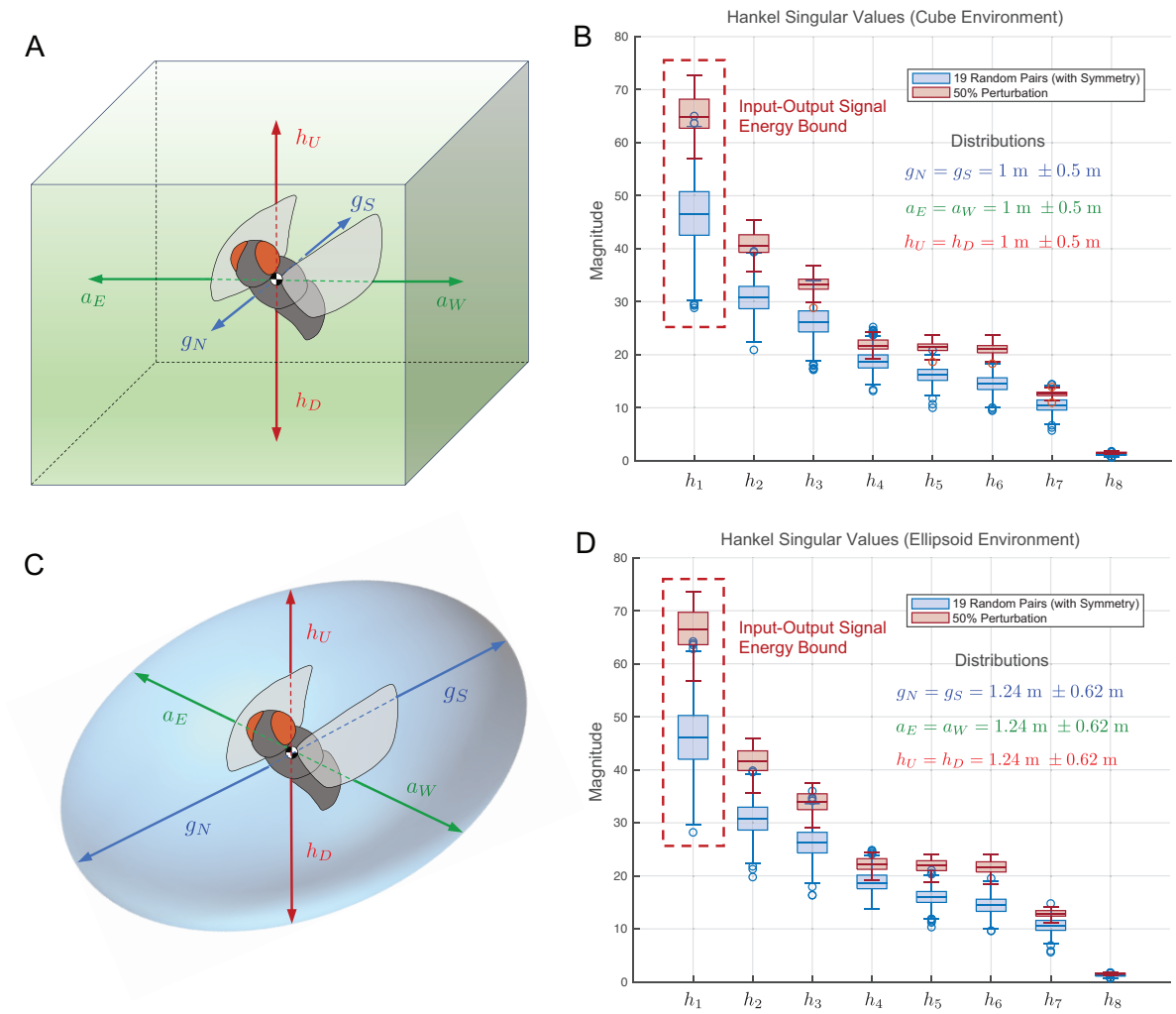

Fig. 7 Robustness of Hankel singular values to environment perturbations. The dimensions $(g_N, g_S, a_E, a_W, h_u, h_d)$ of two different nominal environment configurations with equal volume (cube, ellipsoid) are randomly selected from a uniform distribution (100 different configurations each) up to 50% and used to generate the system's Hankel singular values. These distributions are compared to 1000 sets of randomly selected 19 left-right symmetric pairs from a uniform distribution on $\mathbb{R}^8$. (A) Geometry of the cube environment. (B) Comparison of Hankel singular values for 100 randomly selected cube environment configurations. (C) Geometry of the ellipsoid environment. (D) Comparison of Hankel singular values for 100 randomly selected ellipsoid environment configurations.

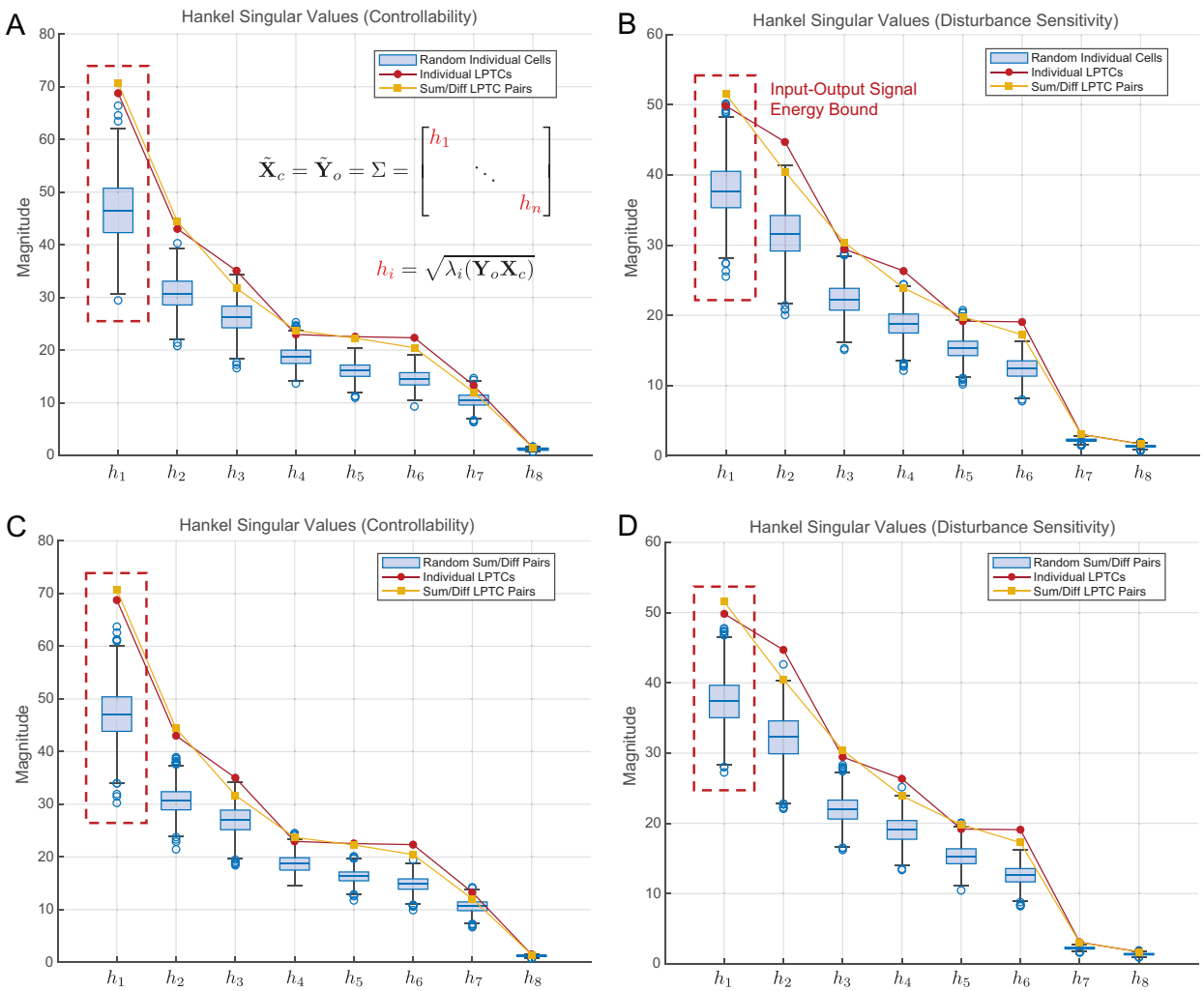

Fig. 8 Hankel singular value dependence on LPTC configuration. Two different configurations (individual cells or bilaterally summed and differenced pairs) of the output vectors $\mathbf{y}'$ and $\mathbf{y}$ respectively are used to generate Hankel singular values for the controllability and disturbance sensitivity cases. These results are compared to two configurations (individual cells or bilaterally summed and differenced pairs) of 1000 randomly generated sets from a uniform distribution on $\mathbb{R}^8$. The maximum Hankel singular value h_1 represents a bound on signal energy transfer from input to output. (A-B) Comparison of Hankel singular values based on the controllability Gramian $\mathbf{X}_c$ and the disturbance sensitivity Gramian $\mathbf{X}_d$ with randomly generated sets of 38 individual cells (19 symmetric pairs). (C-D) Comparison of Hankel singular values based on the controllability Gramian $\mathbf{X}_c$ and the disturbance sensitivity Gramian $\mathbf{X}_d$ with randomly generated sets of bilaterally summed and differenced pairs.

Tables

Table 1 Moments of inertia about the principal axes of *Calliphora vicina* estimated from μCT images.

Insect	m (10^{-5} kg)	I_1 (10^{-10} kg m^2)	I_2 (10^{-10} kg m^2)	I_3 (10^{-10} kg m^2)
male 1	6.792	5.802	5.730	1.457
male 2	7.543	6.410	6.368	1.594
female 1	7.953	6.924	6.883	1.822

Table 2 *Calliphora vicina* flapping wing simulation parameters.

Freestream velocity U_∞ (m s^{-1})	0.8509
Body pitch angle (°) θ_e	30.365
Nominal wing beat frequency (Hz)	166.188
Wing span (mm)	10.1781
Mean chord (mm)	2.714
Reynolds number	1,746

Table 3 CFD Simulation setup parameters.

Total timesteps	2,880 (720 steps per cycle)
Flow condition	Laminar
Spatial reconstruction	5th order WENO scheme
Temporal scheme	2nd order backward difference (BDF2)
Low-Mach precondition	Yes
Overset grid node points	Wing (2.98 M) and Background (8.21 M)

Table 4 Estimated stability derivatives (S.I. units).

X Force (10^{-5})	Z Force (10^{-5})	M Moment (10^{-7})
$X_u = -8.3476$	$Z_u = -14.009$	$M_u = 2.2833$
$X_w = 12.690$	$Z_w = -13.499$	$M_w = 1.4421$
$X_q = -0.0286$	$Z_q = -0.0345$	$M_q = -0.0202$
Y Force (10^{-5})	L Moment (10^{-7})	N Moment (10^{-7})
$Y_v = -11.244$	$L_v = 0.7428$	$N_v = 3.1378$
$Y_p = -0.0298$	$L_p = -0.0884$	$N_p = -0.0523$
$Y_r = 0.0159$	$L_r = 0.0968$	$N_r = -0.0132$

Table 5 Estimated control derivatives (S.I. units).

X Force (10^{-5})	Z Force (10^{-5})	M Moment (10^{-7})
$X_{u_0} = 0.4825$	$Z_{u_0} = -0.4428$	$M_{u_0} = -0.0216$
$X_{u_1} = -0.9232$	$Z_{u_1} = 0.2194$	$M_{u_1} = 1.7264$
$X_{u_2} = 1.8744$	$Z_{u_2} = 0.9314$	$M_{u_2} = 0.0312$
$X_{u_3} = -1.6088$	$Z_{u_3} = 2.5656$	$M_{u_3} = 0.6669$
$X_{u_4} = -4.3350$	$Z_{u_4} = -0.5456$	$M_{u_4} = -0.9728$
Y Force (10^{-5})	L Moment (10^{-7})	N Moment (10^{-7})
$Y_{u'_1} = -2.6166$	$L_{u'_1} = 0.0387$	$N_{u'_0} = 1.6863$
$Y_{u'_2} = -0.6990$	$L_{u'_2} = 0.8287$	$N_{u'_1} = -2.1978$
$Y_{u'_3} = -0.2323$	$L_{u'_3} = 0.9588$	$N_{u'_2} = 1.0856$
$Y_{u'_4} = -4.0104$	$L_{u'_4} = 0.5929$	$N_{u'_3} = 2.5151$

Table 6 Eigenstructure of the symmetric and asymmetric modes of the system matrix $\mathbf{A} = \mathbf{A}_S$, showing the eigenvalues (λ_i) and eigenvectors for the symmetric and asymmetric parts, $\mathbf{x}_{\text{long}} = [\delta u\ \delta w\ \delta q\ \delta\theta]^T$ and $\mathbf{x}_{\text{lat}} = [\delta v\ \delta p\ \delta\phi\ \delta r]^T$, of the state vector $\mathbf{x}$ (S.I. units).

symmetric	mode 1	mode 2	mode 3	asymmetric	mode 4	mode 5	mode 6
λ_j	-19.89	$6.77 \pm 14.92j$	-2.28	λ_j	-63.38	-20.16 ± 21.72	15.51
δu	0.0215	$-0.0172 \pm 0.0244j$	0.0317	δv	-0.0017	$0.0012 \pm 0.0149j$	0.0285
δw	0.0506	$-0.0200 \pm 0.0417j$	-0.9042	δp	0.9539	$-0.9927 \pm 0.000j$	0.9852
δp	-0.9972	$-0.9966 \pm 0.000j$	0.3900	$\delta\phi$	-0.0202	$0.0306 \pm 0.0330j$	0.0853
$\delta\theta$	0.0501	$-0.0251 \pm 0.0554j$	-0.1710	δr	-0.2993	$-0.0891 \pm 0.0658j$	0.1458

Table 7 State encoding of the LPTC response fields expressed in the stability axes $\mathcal{S}$ for the baseline enclosed rectangular prism. The rows of the output matrix $\mathbf{C}'$ are formed from the elements corresponding to the motion state variables $\{\delta u_s, \delta w_s, \delta q_s, \delta\theta_s, \delta v_s, \delta p_s, \delta\phi_s, \delta r_s\}$ scaled in S.I. units.

LPTC	δx	δy	δz	$\delta\phi_s$	$\delta\theta_s$	$\delta\psi_s$	δu_s	δv_s	δw_s	δp_s	δq_s	δr_s
Right VS1	0.0036	-0.2905	0.3333	0.0615	0.0363	-0.0123	-0.9072	0.2165	-0.8989	-0.5693	1.5552	1.0170
Left VS1	0.0036	0.2834	0.3333	-0.0650	0.0363	-0.0019	-0.9072	-0.2165	-0.8989	0.5693	1.5552	-1.0170
Right VS2	-0.0420	-0.1251	0.1547	0.0194	0.0509	-0.0163	-0.4123	-0.0721	-1.2885	-0.7610	1.3823	0.2665
Left VS2	-0.0420	0.1219	0.1547	-0.0209	0.0509	0.0100	-0.4123	0.0721	-1.2885	0.7610	1.3823	-0.2665
Right VS3	-0.0528	-0.0978	0.1440	0.0222	0.0109	-0.0096	-0.3498	-0.2108	-1.3341	-1.3619	1.0646	0.1347
Left VS3	-0.0528	0.0953	0.1440	-0.0235	0.0109	0.0048	-0.3498	0.2108	-1.3341	1.3619	1.0646	-0.1347
Right VS4	-0.0221	-0.1161	0.0972	0.0157	-0.0064	-0.0152	-0.3132	-0.3778	-1.4329	-1.7489	0.6139	0.1737
Left VS4	-0.0221	0.1141	0.0972	-0.0168	-0.0064	0.0113	-0.3132	0.3778	-1.4329	1.7489	0.6139	-0.1737
Right VS5	-0.0153	-0.0734	0.0495	0.0128	-0.0101	-0.0094	-0.1959	-0.3875	-1.3851	-1.8758	0.3177	0.0675
Left VS5	-0.0153	0.0723	0.0495	-0.0135	-0.0101	0.0073	-0.1959	0.3875	-1.3851	1.8758	0.3177	-0.0675
Right VS6	-0.0058	-0.1077	0.0066	-0.0046	-0.0039	-0.0027	-0.2074	-0.4018	-1.4020	-1.9090	0.0672	0.1874
Left VS6	-0.0058	0.1064	0.0066	0.0039	-0.0039	0.0002	-0.2074	0.4018	-1.4020	1.9090	0.0672	-0.1874
Right VS7	0.0125	-0.0771	-0.1545	-0.0256	-0.0040	0.0037	-0.0717	-0.3722	-1.3038	-1.8316	-0.6962	0.0666
Left VS7	0.0125	0.0763	-0.1545	0.0252	-0.0040	-0.0053	-0.0717	0.3722	-1.3038	1.8316	-0.6962	-0.0666
Right VS8	0.0151	-0.0177	-0.2970	-0.0471	-0.0017	-0.0009	0.1358	-0.4590	-1.0575	-1.5302	-1.2798	-0.0725
Left VS8	0.0151	0.0174	-0.2970	0.0471	-0.0017	0.0003	0.1358	0.4590	-1.0575	1.5302	-1.2798	0.0725
Right VS9	0.0240	-0.0542	-0.3387	-0.0579	0.0075	-0.0070	0.0909	-0.4091	-1.0339	-1.4136	-1.4151	0.1328
Left VS9	0.0240	0.0524	-0.3387	0.0573	0.0075	0.0034	0.0909	0.4091	-1.0339	1.4136	-1.4151	-0.1328
Right VS10	0.0009	-0.0236	-0.3668	-0.0643	0.0033	-0.0053	0.1981	-0.2682	-0.9965	-1.2382	-1.6187	-0.0305
Left VS10	0.0009	0.0234	-0.3668	0.0643	0.0033	0.0049	0.1981	0.2682	-0.9965	1.2382	-1.6187	0.0305
Right V1	0.0234	-0.1041	0.2121	0.0349	0.0247	-0.0169	-0.3188	-0.2607	-1.3244	-1.2274	1.3058	0.0847
Left V1	0.0234	0.1023	0.2121	-0.0359	0.0247	0.0133	-0.3188	0.2607	-1.3244	1.2274	1.3058	-0.0847
Right V2	-0.0077	-0.1127	0.1101	0.0196	0.0054	0.0032	-0.3405	0.5157	1.3354	1.8181	0.3159	0.4259
Left V2	-0.0077	0.1098	0.1101	-0.0209	0.0054	-0.0090	-0.3405	-0.5157	1.3354	-1.8181	0.3159	-0.4259
Right Vx	0.0553	0.1497	-0.3876	-0.0653	-0.0057	-0.0110	0.6400	-0.4264	-0.7994	-1.2030	-1.4634	-0.5821
Left Vx	0.0553	-0.1459	-0.3876	0.0674	-0.0057	0.0186	0.6400	0.4264	-0.7994	1.2030	-1.4634	0.5821
Right HSN	0.0851	0.3958	-0.3013	-0.0282	-0.0090	-0.0091	1.0810	-0.6088	-0.2585	-0.6068	-1.0442	-1.5361
Left HSN	0.0851	-0.3853	-0.3013	0.0331	-0.0090	0.0298	1.0810	0.6088	-0.2585	0.6068	-1.0442	1.5361
Right HSE	0.0723	0.5727	-0.0222	-0.0044	0.0013	-0.0115	1.1854	-0.5834	-0.0952	-0.1259	-0.1389	-1.9792
Left HSE	0.0723	-0.5571	-0.0222	0.0107	0.0013	0.0423	1.1854	0.5834	-0.0952	0.1259	-0.1389	1.9792
Right HSS	0.1073	0.3172	0.3514	0.0390	-0.0160	-0.0070	1.1466	-0.5377	-0.2360	0.0990	0.8439	-1.2313
Left HSS	0.1073	-0.3068	0.3514	-0.0339	-0.0160	0.0276	1.1466	0.5377	-0.2360	-0.0990	0.8439	1.2313
Right H1	-0.1008	-0.6388	0.0341	0.0063	0.0091	0.0060	-1.2827	0.5117	-0.2298	-0.2709	0.1157	1.9602
Left H1	-0.1008	0.6224	0.0341	-0.0132	0.0091	-0.0385	-1.2827	-0.5117	-0.2298	0.2709	0.1157	-1.9602
Right H2	-0.1925	-0.3678	0.0237	0.0059	-0.0022	0.0325	-0.8307	0.8135	-0.1704	-0.1362	0.1575	1.6765
Left H2	-0.1925	0.3553	0.0237	-0.0108	-0.0022	-0.0571	-0.8307	-0.8135	-0.1704	0.1362	0.1575	-1.6765
Right Hx	-0.1144	-0.4909	-0.0475	0.0060	-0.0196	-0.0385	-1.2660	1.1101	-0.0775	-0.2646	-0.1093	1.4931
Left Hx	-0.1144	0.4808	-0.0475	-0.0107	-0.0196	0.0187	-1.2660	-1.1101	-0.0775	0.2646	-0.1093	-1.4931

Supplementary information

Flight dynamics modelling

As outlined in the main text, we have parameterized a linear time-invariant (LTI) flight dynamics model:

$$[\dot{\mathbf{x}}]_{\mathcal{B}}(t) = \mathbf{A}_{\mathcal{B}}[\mathbf{x}]_{\mathcal{B}}(t) + \mathbf{B}_{\mathcal{B}}\mathbf{u}(t) + \mathbf{G}_{\mathcal{B}}[\mathbf{d}]_{\mathcal{B}}(t), \tag{9}$$

where the state vector $[\mathbf{x}]_{\mathcal{B}} = [\delta u\ \delta w\ \delta q\ \delta\theta\ \delta v\ \delta p\ \delta\phi\ \delta r]^T$ is sufficient to describe the 6-DoF rigid body motions of the insect insofar as these motions influence the wingbeat-averaged aerodynamic forces $\{X, Y, Z\}$ and moments $\{L, M, N\}$ resolved in the principal axes of the body $\mathcal{B} = \{\hat{\boldsymbol{x}}_b, \hat{\boldsymbol{y}}_b, \hat{\boldsymbol{z}}_b\}$ as described in Ext. Data Fig. 6. Here, δ denotes a small perturbation from equilibrium, where $\{u, v, w\}$ are the components of translational velocity along the principal axes of the body, where $\{p, q, r\}$ are the components of angular velocity about these body axes, and where $\{\theta, \phi\}$ are the pitch and bank angles of the insect. These Euler angles are defined as the second and third rotations in an intrinsic 3-2-1 rotation sequence bringing the body axes to their final orientation, starting from an initial configuration in which the z-axis is vertical. Note that the first Euler angle describing the azimuth ψ about the body z-axis is not included in the system state, because it has no influence on the flight physics.

The linearization of the equations of motion for a rigid flying body using small perturbation theory is dealt with in most flight dynamics texts, so is not repeated here. In brief, we modeled the insect as a symmetric rigid body subject to wingbeat-averaged aerodynamic forces and moments. These are described as linear functions of the motion state variables $\{u, v, w, p, q, r\}$ and longitudinal and lateral control input variables $\mathbf{u}_{\text{long}} = [u_0\ u_1\ u_2\ u_3\ u_4]^T$ and $\mathbf{u}_{\text{lat}} = [u'_1\ u'_2\ u'_3\ u'_4]^T$ for small perturbations from a symmetric rectilinear equilibrium flight condition. See [21, 37, 39] for discussion of this approach in the context of insect flight dynamics, including the wingbeat-averaging of the aerodynamic forces and moments, which is an approach borrowed from simplified helicopter flight dynamics modeling. In the following, we assume that the relevant quantities are all expressed in the body frame $\mathcal{B}$, and therefore drop the coordinate frame notation $\mathcal{B}$ hereafter.

With these definitions and assumptions, we model the longitudinal flight dynamics $\dot{\mathbf{x}}_{\text{long}}(t) = \mathbf{A}_{\text{long}}\mathbf{x}_{\text{long}}(t) + \mathbf{B}_{\text{long}}\mathbf{u}_{\text{long}}(t)$ as

$$\begin{bmatrix} \delta\dot{u} \\ \delta\dot{w} \\ \delta\dot{q} \\ \delta\dot{\theta} \end{bmatrix} = \begin{bmatrix} \frac{X_u}{m} & \frac{X_w}{m} & \frac{X_q}{m} - w_e & -g\cos\theta_e \\ \frac{Z_u}{m} & \frac{Z_w}{m} & \frac{Z_q}{m} + u_e & -g\sin\theta_e \\ \frac{M_u}{I_y} & \frac{M_w}{I_y} & \frac{M_q}{I_y} & 0 \\ 0 & 0 & 1 & 0 \end{bmatrix} \begin{bmatrix} \delta u \\ \delta w \\ \delta q \\ \delta\theta \end{bmatrix} + \begin{bmatrix} \frac{X_{u_0}}{m} & \frac{X_{u_1}}{m} & \cdots & \frac{X_{u_4}}{m} \\ \frac{Z_{u_0}}{m} & \frac{Z_{u_1}}{m} & \cdots & \frac{Z_{u_4}}{m} \\ \frac{M_{u_0}}{I_y} & \frac{M_{u_1}}{I_y} & \cdots & \frac{M_{u_4}}{I_y} \\ 0 & 0 & \cdots & 0 \end{bmatrix} \begin{bmatrix} u_0 \\ u_1 \\ \vdots \\ u_4 \end{bmatrix},$$

where $\{u_e, w_e, \theta_e\}$ are the values of $\{u, w, \theta\}$ at equilibrium, where g is gravitational acceleration, m is body mass, and I_y is the moment of inertia about the body y-axis. Here the control input u_0 denotes a change of wingbeat frequency with respect to equilibrium, whilst the remaining control inputs $\{u_1, \cdots, u_4\}$ denote mirror-symmetric application of the time-periodic kinematic couplings in the directions defined by PC1 through to PC4 (see Methods). Quantities of the form X_u, Z_w, M_q, etc. are stability derivatives, denoting the partial derivatives $\partial X/\partial u$, $\partial Z/\partial w$, $\partial M/\partial q$, etc.

Likewise, quantities of the form X_{u_o}, Z_{u_1}, M_{u_4}, etc., are control derivatives, denoting the partial derivatives $\partial X/\partial u_0, \partial Z/\partial u_1, \partial M/\partial u_4$, etc. Derivatives were estimated by regressing the wingbeat-averaged forces and moments predicted using CFD on the relevant state variables and control input variables (see Methods). Note that for the purposes of the flight dynamics modeling described here, we regress the perturbed forces and moments on the perturbed state variables and control input variables, and therefore force the regressions through the origin.

If we assume that external gusts $\mathbf{d}(t) = \{u_d, v_d, w_d, p_d, q_d, r_d\}$ are acting on the animal, then we may replace the motion state variables $\{u, v, w, p, q, r\}$ used to calculate the aerodynamic forces and moments ($\Delta X, \Delta M$, etc.) with an inertial perturbation and a disturbance term, such that $\delta u_a = \delta u - u_d$, $\delta r_a = \delta r - r_d$, etc. Under this assumption, the forces and moments on the insect are now a function of both the inertial and the gust components. For instance,

$$\Delta X = \frac{\partial X}{\partial u}\delta u_a = \frac{\partial X}{\partial u}(\delta u - u_d) = \frac{\partial X}{\partial u}\delta u - \frac{\partial X}{\partial u}u_d.$$

Therefore the way the gust u_d influences the dynamics $\dot{\mathbf{x}}$ is through the term $-\partial X/\partial u$, which is the negative of the aerodynamic portions of the $\mathbf{A}$ matrix. The longitudinal flight dynamics model with gusts are then modeled as $\dot{\mathbf{x}} = \mathbf{A}_{\text{long}}\mathbf{x}(t) + \mathbf{G}_{\text{long}}\mathbf{d}_{\text{long}}(t)$ with

$$\mathbf{G}_{\text{long}} = \begin{bmatrix} -\frac{X_u}{m} & -\frac{X_w}{m} & -\frac{X_q}{m} \\ -\frac{Z_u}{m} & -\frac{Z_w}{m} & -\frac{Z_q}{m} \\ -\frac{M_u}{I_y} & -\frac{M_w}{I_y} & -\frac{M_q}{I_y} \\ 0 & 0 & 0 \end{bmatrix} \text{ and } \mathbf{d}_{\text{long}} = \begin{bmatrix} u_d \\ w_d \\ q_d \end{bmatrix}.$$

The lateral flight dynamics $\dot{\mathbf{x}}_{\text{lat}}(t) = \mathbf{A}_{\text{lat}}\mathbf{x}_{\text{lat}}(t) + \mathbf{B}_{\text{lat}}\mathbf{u}_{\text{lat}}(t)$ are modeled as

$$\begin{bmatrix} \delta\dot{v} \\ \delta\dot{p} \\ \delta\dot{\phi} \\ \delta\dot{r} \end{bmatrix} = \begin{bmatrix} \frac{Y_v}{m} & \frac{Y_p}{m} + w_e & g\cos\theta_e & \frac{Y_r}{m} - u_e \\ \frac{L_v}{I_x} & \frac{L_p}{I_x} & 0 & \frac{L_r}{I_x} \\ 0 & 1 & 0 & \tan\theta_e \\ \frac{N_v}{I_z} & \frac{N_p}{I_z} & 0 & \frac{N_r}{I_z} \end{bmatrix} \begin{bmatrix} \delta v \\ \delta p \\ \delta\phi \\ \delta r \end{bmatrix} + \begin{bmatrix} \frac{Y_{u'_1}}{m} & \frac{Y_{u'_2}}{m} & \frac{Y_{u'_3}}{m} & \frac{Y_{u'_4}}{m} \\ \frac{L_{u'_1}}{I_x} & \frac{L_{u'_2}}{I_x} & \frac{L_{u'_3}}{I_x} & \frac{L_{u'_4}}{I_x} \\ 0 & 0 & 0 & 0 \\ \frac{N_{u'_1}}{I_z} & \frac{N_{u'_2}}{I_z} & \frac{N_{u'_3}}{I_z} & \frac{N_{u'_4}}{I_z} \end{bmatrix} \begin{bmatrix} u'_1 \\ u'_2 \\ u'_3 \\ u'_4 \end{bmatrix},$$

where the notation is similar, save that the control inputs $\{u'_1, \cdots, u'_4\}$ denote anti-symmetric application of the time-periodic kinematic couplings in the directions defined by PC1 through to PC4 (see Methods). The lateral flight dynamics model with gusts $\dot{\mathbf{x}}_{\text{lat}}(t) = \mathbf{A}_{\text{lat}}\mathbf{x}_{\text{lat}}(t) + \mathbf{G}_{\text{lat}}\mathbf{d}_{\text{lat}}(t)$ is derived in the same way as its longitudinal counterpart, with

$$\mathbf{G}_{\text{lat}} = \begin{bmatrix} -\frac{Y_v}{m} & -\frac{Y_p}{m} & -\frac{Y_r}{m} \\ -\frac{L_v}{I_x} & -\frac{L_p}{I_x} & -\frac{L_r}{I_x} \\ -\frac{N_v}{I_z} & -\frac{N_p}{I_z} & -\frac{N_r}{I_z} \\ 0 & 0 & 0 \end{bmatrix} \text{ and } \mathbf{d}_{\text{lat}} = \begin{bmatrix} v_d \\ p_d \\ r_d \end{bmatrix}.$$

Note that these equations of motion are linearized about a symmetric rectilinear equilibrium flight condition with $v_e = p_e = q_e = r_e = \phi_e = 0$, and neglect any gyroscopic forces on the beating wings. They further assume that the fastest natural modes of the system have a characteristic timescale much longer than the period of the wingbeat, such that there is no significant coupling between the time-periodic oscillations of the aerodynamic forces and the body's motion. It is important to note that their simplified form reflects the fact that all of the forces and moments are resolved with respect to the principal axes of the insect. Finally, although we do not derive the LTI model of the flight dynamics explicitly above, another key feature of this model is that it is linearized about a state of equilibrium, which is a necessary condition for time-invariant equations of motion to result from the linearization.

Whilst it is reasonable to assume that the reference flight condition associated with the mean wingbeat in the functional principal components analysis will be close to equilibrium, there is no reason to expect that it will be exactly so. To guarantee the internal consistency of the model, we therefore enforce equilibrium, subject to the assumption: (i) that $v_e = p_e = q_e = r_e = \phi_e = 0$ on grounds of symmetry; and (ii) that $\{u_e, w_e, \theta_e\}$ are each equal to the reference conditions assumed in the CFD modeling. We achieve this by making three assumptions. First, we assume that the magnitude of the vertical aerodynamic force predicted by the CFD under the reference flight conditions is exactly balanced by the insect's body weight. We therefore solve for the value of body mass at which this assumption holds and set m equal to this value (5.7686×10^{-5} kg) in the flight dynamics model. Second, we assume that the net thrust predicted by the CFD under the reference flight conditions is exactly balanced by body drag in forward flight. This body drag does not feature explicitly in the flight dynamics model, because it is implicit in the treatment of the reference flight conditions from the CFD as an equilibrium condition. Third, noting that the aerodynamic moments predicted by the CFD are resolved at the root of the wing, we assume that any non-zero pitching moment about the wing root is balanced at the centre of mass by the vertical aerodynamic force. We therefore solve for the horizontal lever arm in the xz-plane for which this assumption holds and assume that the wing root is located on a known transverse lever arm along the y-axis that we measure directly from the tomograms (see Methods). Finally, we resolve all of the aerodynamic moments at the centre of mass prior to taking the stability and control derivatives above.

With these assumptions and parameterizations, the longitudinal and lateral **A**, **B**, and **G** matrices for a freestream velocity of $U_\infty = 0.8509$ m/s and a body pitch angle $\theta_e = 30.365°$ expressed in the body frame $\mathcal{B}$ for *Calliphora vicina* are as follows, in S.I. units:

$$\mathbf{A}_{\text{long}} = \begin{bmatrix} -1.4471 & 2.1998 & -0.4351 & -8.4614 \\ -2.4284 & -2.3400 & 0.7282 & -4.9573 \\ 547.09 & 345.54 & -4.8501 & 0 \\ 0 & 0 & 1 & 0 \end{bmatrix}$$

$$\mathbf{A}_{\text{lat}} = \begin{bmatrix} -1.9492 & 0.4250 & 8.4614 & -0.7314 \\ 697.24 & -83.067 & 0 & 90.875 \\ 0 & 1 & 0 & 0.5859 \\ 751.82 & -12.546 & 0 & -3.1760 \end{bmatrix}$$

$$\mathbf{B}_{\text{long}} = \begin{bmatrix} 0.0837 & -0.1600 & 0.3249 & -0.2789 & -0.7515 \\ -0.0768 & 0.0380 & 0.1615 & 0.4448 & -0.0946 \\ -5.1932 & 413.65 & 74.900 & 159.80 & -233.11 \\ 0 & 0 & 0 & 0 & 0 \end{bmatrix}$$

$$\mathbf{B}_{\text{lat}} = \begin{bmatrix} -0.4536 & -0.1212 & -0.0403 & -0.6952 \\ 36.391 & 777.94 & 900.06 & 556.56 \\ 404.05 & -526.60 & 260.11 & 602.64 \\ 0 & 0 & 0 & 0 \end{bmatrix}$$

$$\mathbf{G}_{\text{long}} = \begin{bmatrix} 1.4471 & -2.1998 & 0.0050 \\ 2.4284 & 2.3400 & 0.0060 \\ -547.09 & -345.54 & 4.8501 \\ 0 & 0 & 0 \end{bmatrix}$$

$$\mathbf{G}_{\text{lat}} = \begin{bmatrix} 1.9492 & 0.0051 & -0.0028 \\ -697.24 & 83.067 & -90.875 \\ 0 & 0 & 0 \\ -751.82 & 12.546 & 3.1760 \end{bmatrix}$$

Writing the equations of motion in the body frame $\mathcal{B}$ as above results in a simpler form than that which is obtained when using an axis system that is not necessarily aligned with the principal axes of the body. On the other hand, the visual axes of the head $\mathcal{H}$ do not in general coincide with the principal axes of the body at equilibrium, and it is more reasonable to assume that the head is held level at equilibrium such that the retinal coordinates (0,0) coincide with the insect's velocity vector in level flight at equilibrium. The set of body-fixed axes whose x-axis is aligned with the insect's velocity vector at equilibrium, and whose transverse y-axis is normal to the insect's plane of symmetry, is called the stability axis system $\mathcal{S}$. In a final step, we therefore transform the equations of motion above from the body axes $\mathcal{B}$ into the stability axes $\mathcal{S}$, which simplifies the analysis in the main text. The details of these coordinate transformations are described further below.

Coordinate Frames

Three different coordinate frames are employed in the preceding analyses (Ext. Data Fig. 6A): (i) the head (visual) axes $\mathcal{H} = \{\hat{\boldsymbol{x}}_h, \hat{\boldsymbol{y}}_h, \hat{\boldsymbol{z}}_h\}$, (ii) the body (principal) axes $\mathcal{B} = \{\hat{\boldsymbol{x}}_b, \hat{\boldsymbol{y}}_b, \hat{\boldsymbol{z}}_b\}$, and the stability axes $\mathcal{S} = \{\hat{\boldsymbol{x}}_s, \hat{\boldsymbol{y}}_s, \hat{\boldsymbol{z}}_s\}$. The visual $\mathcal{H}$ axes and the body $\mathcal{B}$ axes are defined anatomically, whereas the stability $\mathcal{S}$ axes are specified by orienting the $\boldsymbol{x}_s$ direction along the relative velocity vector for the given reference flight condition. The body axes $\mathcal{B}$ are the natural coordinate frame in which to calculate the variations in the aerodynamic forces $\{X, Y, Z\}$ and moments $\{L, M, N\}$, as the results can be straightforwardly transformed to stability axes $\mathcal{S}$ for an arbitrary reference flight condition. Furthermore, because it assumed that the directions of the visual axes $\mathcal{H}$ and the stability axes $\mathcal{S}$ are aligned, the natural coordinate frame in which to express the flight dynamics and sensor outputs (Eqs. 1-2) is the stability frame $\mathcal{S}$:

$$[\dot{\mathbf{x}}]_{\mathcal{S}}(t) = \mathbf{A}_{\mathcal{S}}[\mathbf{x}]_{\mathcal{S}}(t) + \mathbf{B}_{\mathcal{S}}\mathbf{u}(t) + \mathbf{G}_{\mathcal{S}}[\mathbf{d}]_{\mathcal{S}}(t) \tag{10}$$

$$\mathbf{y}(t) = \mathbf{C}_{\mathcal{S}}[\mathbf{x}]_{\mathcal{S}}(t). \tag{11}$$

Bracket notation and subscripts are used to denote the coordinate frame for which a specific vector or matrix is expressed. In particular, $[\mathbf{x}]_S = [\delta u_s\ \delta w_s\ \delta q_s\ \delta\theta_s\ \delta v_s\ \delta p_s\ \delta\phi_s\ \delta r_s]^T$ is the perturbation state expressed in stability coordinates, $[\mathbf{d}]_S = [u_{d,s}\ w_{d,s}\ q_{d,s}\ v_{d,s}\ p_{d,s}\ r_{d,s}]^T$ are the gust inputs in stability coordinates, and the entries of the $\mathbf{A}_\mathcal{S}$, $\mathbf{B}_\mathcal{S}$, $\mathbf{G}_\mathcal{S}$, and $\mathbf{C}_\mathcal{S}$ system matrices are relative to the stability axes.

The electrophysiological characterization of LPTC response field properties was performed relative to the visual (head) axes $\mathcal{H}$, whose directions correspond to the stability axes $\mathcal{S}$, therefore $\mathbf{C}_\mathcal{S} = \mathbf{C}_\mathcal{H}$. The CFD characterizations of perturbation forces and moments (matrices $\mathbf{A}_\mathcal{B}$, $\mathbf{B}_\mathcal{B}$, and $\mathbf{G}_\mathcal{B}$) were generated relative to the body axes $\mathcal{B}$, so a transformation of the $[\mathbf{x}]_\mathcal{B}$ and $[\mathbf{d}]_\mathcal{B}$ vectors into stability axes $\mathcal{S}$ is required to put the system into the form of Eqn. 10 to perform a comparison between the directions encoded by the LPTCs and the dynamically-significant directions defined by the Gramians.

To derive these transformations, we first consider the relationship between the velocity $\mathbf{v}$ and angular velocity $\boldsymbol{\omega}$ in these two coordinate frames, which differ by a rotation θ_e about the pitch axis (Ext. Data Fig. 6):

$$R_{\mathcal{BS}}(\theta_e) = \begin{pmatrix} \cos\theta_e & 0 & -\sin\theta_e \\ 0 & 1 & 0 \\ \sin\theta_e & 0 & \cos\theta_e \end{pmatrix} \tag{12}$$

Hence, the velocity of the animal in body coordinates $[\mathbf{v}]_B$ is related to its velocity in stability coordinates $[\mathbf{v}]_S$ via

$$[\mathbf{v}]_B = \begin{pmatrix} u \\ v \\ w \end{pmatrix} = R_{\mathcal{BS}}(\theta_e)\ [\mathbf{v}]_S = \begin{pmatrix} \cos\theta_e & 0 & -\sin\theta_e \\ 0 & 1 & 0 \\ \sin\theta_e & 0 & \cos\theta_e \end{pmatrix} \begin{pmatrix} u_s \\ v_s \\ w_s \end{pmatrix}. \tag{13}$$

Similarly, the angular velocity of the animal in body coordinates $[\boldsymbol{\omega}]_B$ is related to its velocity in stability coordinates $[\boldsymbol{\omega}]_S$ via

$$[\boldsymbol{\omega}]_B = \begin{pmatrix} p \\ q \\ r \end{pmatrix} = R_{\mathcal{BS}}(\theta_e)\ [\boldsymbol{\omega}]_S = \begin{pmatrix} \cos\theta_e & 0 & -\sin\theta_e \\ 0 & 1 & 0 \\ \sin\theta_e & 0 & \cos\theta_e \end{pmatrix} \begin{pmatrix} p_s \\ q_s \\ r_s \end{pmatrix}. \tag{14}$$

The full 8-dimensional state vector expressed in the body frame also contains two attitude angles, θ and ϕ. In the linearized flight dynamics these are actually perturbation angles from equilibrium, hence $\theta = \theta_s$ since the $\hat{\boldsymbol{y}}_b$ and $\hat{\boldsymbol{y}}_s$ coordinate axes are colinear. To develop the relationship between ϕ and ϕ_s, we take the axis-angle form for a rotation ϕ_s about the $\hat{\boldsymbol{x}}_s$ axis expressed in the $\mathcal{B} = \{\hat{\boldsymbol{x}}_b, \hat{\boldsymbol{y}}_b, \hat{\boldsymbol{z}}_b\}$ coordinate frame, convert this to its equivalent rotation matrix, then back out the equivalent 3-2-1 Euler angles $\{\phi, \theta, \psi\}$ referred to the body $\mathcal{B}$ frame. The axis-angle form is angle ϕ_s about axis $\hat{\mathbf{e}} = (\cos\theta_e, 0, \sin\theta_e)$. If we equate the corresponding rotation matrix for ϕ_s and $\hat{\mathbf{e}}$ with the 3-2-1 Euler angle parameterization in body axes $\{\phi, \theta, \psi\}$ of the same rotation, a ratio of the (3,2) and (3,3) entries results in

$$\tan\phi = \frac{\cos\theta_e \sin\phi_s}{(1-\cos\phi_s)\sin^2\theta_e + \cos\phi_s}. \tag{15}$$

Hence for small ϕ_s and small ϕ, this reduces to $\phi \approx (\cos\theta_e)\phi_s$.

Therefore, the longitudinal state transformation from stability $\mathcal{S}$ to body axes $\mathcal{B}$ is $[\mathbf{x}_{\text{long}}]_{\mathcal{B}} = R_{\text{long}}[\mathbf{x}_{\text{long}}]_{\mathcal{S}}$ is given by

$$\begin{pmatrix} u \\ w \\ q \\ \theta \end{pmatrix} = \begin{pmatrix} \cos\theta_e & -\sin\theta_e & 0 & 0 \\ \sin\theta_e & \cos\theta_e & 0 & 0 \\ 0 & 0 & 1 & 0 \\ 0 & 0 & 0 & 1 \end{pmatrix} \begin{pmatrix} u_s \\ w_s \\ q_s \\ \theta_s \end{pmatrix}, \tag{16}$$

and the lateral state transformation from stability to body axes $[\mathbf{x}_{\text{lat}}]_{\mathcal{B}} = R_{\text{lat}}[\mathbf{x}_{\text{lat}}]_{\mathcal{S}}$ is given by

$$\begin{pmatrix} v \\ p \\ \phi \\ r \end{pmatrix} = \begin{pmatrix} 1 & 0 & 0 & 0 \\ 0 & \cos\theta_e & 0 & -\sin\theta_e \\ 0 & 0 & \cos\theta_e & 0 \\ 0 & \sin\theta_e & 0 & \cos\theta_e \end{pmatrix} \begin{pmatrix} v_s \\ p_s \\ \phi_s \\ r_s \end{pmatrix}. \tag{17}$$

The transformation for the full state $[\mathbf{x}]_{\mathcal{B}} = R[\mathbf{x}]_{\mathcal{S}}$ (longitudinal and lateral states combined) is

$$R = \begin{pmatrix} R_{\text{long}} & 0 \\ 0 & R_{\text{lat}} \end{pmatrix}. \tag{18}$$

Since the disturbance vector $\mathbf{d}$ has six components compared to the eight components of the state vector $\mathbf{x}$, we also define a transformation R_G which maps components of vectors expressed in the $\mathcal{S}$ frame to the $\mathcal{B}$ frame. This transformation is essentially the R matrix with the rows and columns associated with the θ and ϕ variables removed.

To express the $\mathbf{A}_{\mathcal{B}}$, $\mathbf{B}_{\mathcal{B}}$, and $\mathbf{G}_{\mathcal{B}}$ matrices relative to the stability axes $\mathcal{S}$, we substitute $[\mathbf{x}]_{\mathcal{B}} = R[\mathbf{x}]_{\mathcal{S}}$, $[\dot{\mathbf{x}}]_{\mathcal{B}} = R[\dot{\mathbf{x}}]_{\mathcal{S}}$, and $[\mathbf{d}]_{\mathcal{B}} = R_G[\mathbf{d}]_{\mathcal{S}}$ into $[\dot{\mathbf{x}}]_{\mathcal{B}} = \mathbf{A}_{\mathcal{B}}[\mathbf{x}]_{\mathcal{B}} + \mathbf{B}_{\mathcal{B}}\mathbf{u} + \mathbf{G}_{\mathcal{B}}[\mathbf{d}]_{\mathcal{B}}$,

$$[\dot{\boldsymbol{x}}]_{\mathcal{S}} = R^{-1}\mathbf{A}_{\mathcal{B}}R[\mathbf{x}]_{\mathcal{S}} + R^{-1}\mathbf{B}_{\mathcal{B}}\mathbf{u} + R^{-1}\mathbf{G}_{\mathcal{B}}R_G[\mathbf{d}]_{\mathcal{S}}. \tag{19}$$

The final system matrices $\mathbf{A} = \mathbf{A}_{\mathcal{S}}$, $\mathbf{B} = \mathbf{B}_{\mathcal{S}}$, and $\mathbf{G} = \mathbf{G}_{\mathcal{S}}$ (Eqn. 1), expressed in the stability axes $\mathcal{S}$, are then $\mathbf{A}_{\mathcal{S}} = R^{-1}\mathbf{A}_{\mathcal{B}}R$, $\mathbf{B}_{\mathcal{S}} = R^{-1}\mathbf{B}_{\mathcal{B}}$, and $\mathbf{G}_{\mathcal{S}} = R^{-1}\mathbf{G}_{\mathcal{B}}R_G$. To simplify our notation, we have omitted these $\mathcal{S}$ subscripts in the main text.

Dynamically significant directions in state space

The Gramians constructed from the $\mathbf{A}$, $\mathbf{B}$, and $\mathbf{G}$ system matrices encode the dynamic properties of a system. These matrices have been widely used in testing for controllability and observability [65–67], in model reduction [66, 68–70], in sensor and actuator placement [15, 71–73], in disturbance rejection [74, 75], and in joint sensor and actuator design [76, 77]. When the system matrix $\mathbf{A}$ is stable, the controllability and observability gramians are defined in the time domain as:

$$\mathbf{X}_c = \int_0^\infty e^{\mathbf{A}\tau}\mathbf{B}\mathbf{B}^T e^{\mathbf{A}^T\tau} d\tau \tag{20}$$

$$\mathbf{Y}_o = \int_0^\infty e^{\mathbf{A}^T\tau}\mathbf{C}^T\mathbf{C} e^{\mathbf{A}\tau} d\tau. \tag{21}$$

The disturbance sensitivity Gramian $\mathbf{X}_d$ is constructed similar to $\mathbf{X}_c$, by swapping the $\mathbf{B}$ with the $\mathbf{G}$ matrix in Eqn. 20. The Gramians are generated by computing the solutions to the Lyanunov equations,

$$\mathbf{A}\mathbf{X}_c + \mathbf{X}_c^T\mathbf{A} + \mathbf{B}\mathbf{B}^T = 0 \tag{22}$$

$$\mathbf{A}^T\mathbf{Y}_o + \mathbf{Y}_o\mathbf{A} + \mathbf{C}^T\mathbf{C} = 0. \tag{23}$$

The controllability Gramian has a direct connection with the minimum energy required to reach a given state $\mathbf{x}_0$, which can be expressed as $\|\mathbf{u}_{\text{opt}}\|^2 = \mathbf{x}_0^T\mathbf{X_c}^{-1}\mathbf{x}_0$. By extension, the controllability ellipsoid $\mathcal{E}_c = \{\mathbf{x} \in \mathbb{R}^n;\ \mathbf{x}^T\mathbf{X}_c^{-1}\mathbf{x} \leq 1\}$ contains the region of state space that can be reached by applying inputs with unit norm $\|\mathbf{u}\|_2 \leq 1$ [66]. The principal axes directions and lengths of $\mathcal{E}_c$ are determined by the eigenvectors and square roots of the eigenvalues of $\mathbf{X}_c$. Hence, its longest axes represent the directions in state space requiring the least control effort to move along. Similarly, the disturbance sensitivity ellipsoid ($\mathcal{E}_d$) is constructed in an identical fashion, but with $\mathbf{X}_d$ interchanged with $\mathbf{X}_c$. Its longest axes represent the directions of motion that are most readily excited by gusts. These most-sensitive directions characterise the worst-case disturbances that the insect may have to reject.

The observability Gramian has a direct connection to output energy for a given initial condition $\mathbf{x}_0$, because the energy of the output signal $\mathbf{y}(t)$ for an arbitrary $\mathbf{x}_0$ can be expressed as $\|\mathbf{y}\|^2 = \mathbf{x}_0^T\mathbf{Y_o}\mathbf{x}_0$. If we consider the set of initial conditions where $\|\mathbf{y}\|^2 \leq 1$, this yields the directions in state space that have the smallest output norm. If we replace $\mathbf{Y}_o$ with its inverse, then we can form the observability ellipsoid $\mathcal{E}_o = \{\mathbf{x} \in \mathbb{R}^n; \mathbf{x}^T\mathbf{Y}_o^{-1}\mathbf{x} \leq 1\}$. The principal axes of $\mathcal{E}_o$ represent the directions in state space that yield the largest output norm, characterising the specific self-motions that the insect is best-able to sense. Additionally, $\mathbf{Y}_o^{-1} = E\{[\mathbf{x}(t) - \hat{\mathbf{x}}(t)][\mathbf{x}(t) - \hat{\mathbf{x}}(t)]^T\}$ is the covariance for the best unbiased estimate $\hat{\mathbf{x}}(t)$ based on the measurement $\{\mathbf{y}(t),\ 0 < t < \infty\}$ that minimizes the scalar cost function $J = \text{Tr}(\mathbf{Y}_o^{-1}) = E\{[\mathbf{x}(t) - \hat{\mathbf{x}}(t)]^T[\mathbf{x}(t) - \hat{\mathbf{x}}(t)]\}$. It follows that $\text{Tr}(\mathbf{Y}_o^{-1})$ is a measure of the average estimate covariance of the system [78].

For system matrices $\mathbf{A}$ that are unstable, the integrals in Eqns. 20 and 21 are unbounded and $\mathbf{X}_c$ and $\mathbf{Y}_o$ are undefined. Generalizations to the controllability and observability Gramians were introduced in [43], corresponding to Eqns. 3 and 4 in the main text. For $(\mathbf{A}, \mathbf{B})$ stabilizable, $(\mathbf{C}, \mathbf{A})$ detectable, and no eigenvalues of $\mathbf{A}$ on the imaginary axis, the generalized Gramians are calculated as follows. First compute the solutions $\mathbf{P}$ and $\mathbf{Q}$ to the Riccati equations,

$$\mathbf{A}^T\mathbf{P} + \mathbf{P}\mathbf{A} - \mathbf{P}\mathbf{B}\mathbf{B}^T\mathbf{P} = 0 \tag{24}$$

$$\mathbf{Q}\mathbf{A}^T + \mathbf{A}\mathbf{Q} - \mathbf{Q}\mathbf{C}^T\mathbf{C}\mathbf{Q} = 0. \tag{25}$$

Next define $\mathbf{F} = -\mathbf{B}^T\mathbf{P}$ and $\mathbf{L} = -\mathbf{Q}\mathbf{C}^T$, and the generalized Gramians are the solutions to the Lyapunov equations,

$$(\mathbf{A} + \mathbf{B}\mathbf{F})\mathbf{X}_c + \mathbf{X}_c^T(\mathbf{A} + \mathbf{B}\mathbf{F}) + \mathbf{B}\mathbf{B}^T = 0 \tag{26}$$

$$(\mathbf{A} + \mathbf{L}\mathbf{C})^T\mathbf{Y}_o + \mathbf{Y}_o(\mathbf{A} + \mathbf{L}\mathbf{C}) + \mathbf{C}^T\mathbf{C} = 0. \tag{27}$$

If the $\mathbf{A}$ matrix is stable, then $\mathbf{P} = 0$ and $\mathbf{Q} = 0$, and Eqns. 26 and 27 reduce to Eqns. 22 and 23. The authors in [43] also provide time domain interpretations of the generalized Gramians, and show they can be similarly related to the minimum control energy $\mathbf{x}_0^T\mathbf{X_c}^{-1}\mathbf{x}_0$, the minimum estimation error $\mathbf{Y}_o^{-1}$, and average estimation error $\text{Tr}(\mathbf{Y}_o^{-1})$.

Balanced realization theory for stable linear systems introduced by [68] provides additional tools for understanding the energy flow properties of a dynamical system. In particular, one can quantify the joint controllability and observability of a system that has been transformed into balanced coordinates $\check{\mathbf{x}} = \mathbf{T}\mathbf{x}$, where $\{\hat{\mathbf{t}}_i\}$ denote the columns of $\mathbf{T}^{-1}$. In these new coordinates the controllability

and observability Gramians (Eqns. 20 and 21) are equal and diagonal, $\check{\mathbf{X}}_c = \check{\mathbf{Y}}_o = \mathrm{diag}(h_1, \cdots, h_n)$, where the Hankel singular values $h_i = \sqrt{\mathbf{Y}_o\mathbf{X}_c}$ rank the joint controllability/observability of the direction $\hat{\mathbf{t}}_i$ in original coordinates. In particular, directions with small h_i correspond to directions in state space that are simultaneously difficult to reach and observe, and contribute little to the overall behavior of the system. An extension to the unstable case was provided in [43], who showed that the same tools could be applied through the introduction of the generalized controllability Gramian $\mathbf{X}_c$ and observability Gramian $\mathbf{Y}_o$ as in Eqns. 3 and 4 in the main text. In particular, the Hankel singular values (HSVs) for an unstable system with no eigenvalues on the imaginary axis are the union of the HSVs for the partitioned stable and anti-stable subsystems, with the $\mathbf{A}$ matrix for the anti-stable partition replaced with $-\mathbf{A}$, and these are computed similarly as $h_i = \sqrt{\mathbf{Y}_o\mathbf{X}_c}$. The transformation $\check{\mathbf{x}} = \mathbf{T}\mathbf{x}$ that was used to balance the system was based on the Cholesky factorization of $\mathbf{X}_c = \mathbf{W}\mathbf{W}^*$. The eigenvalue decomposition of $\mathbf{W}^*\mathbf{Y}_o\mathbf{W} = \mathbf{V}\mathbf{\Sigma}\mathbf{V}^*$ is performed, with the resulting balancing transform computed as $\mathbf{T} = \mathbf{\Sigma}^{\frac{1}{2}}\mathbf{V}^*\mathbf{W}^{-1}$.

Supplementary results on the LPTC response fields

The V1-cell (Fig. 1B) shows a strong response to downward image motion over most of its frontolateral visual field, which rotates to become a preference for back-to-front image motion in the upper part of its caudolateral visual field ($90° \leq \gamma \leq 150°$), with vanishing sensitivity below the equator. This qualitative combination of response properties suggests that V1 will be most active during nose-up rotation. The V2-cell (Fig. 1C) responds strongly to upward image motion in the lateral visual field ($45° \leq \gamma \leq 150°$), which gradually changes into a preference for back-to-front image motion in the dorsofrontal visual field ($0° \leq \gamma \leq 45°$) and downwards image motion in the zone of binocular overlap ($-30° \leq \gamma \leq 0°$)(Fig. 1C). The right V2-cell will therefore be active during righthanded roll, with its preferred rotation axis directed ventral relative to the longitudinal roll axis (Fig. 1C). The Vx-cell (Fig. 1F) displays a preference for oblique upward image motion in the upper part of the frontal visual field ($-30° \leq \gamma \leq 30°$), which gradually changes into horizontal front-to-back motion ($30° \leq \gamma \leq 105°$) and becomes maximally sensitive to downward motion in the caudolateral visual field ($105° \leq \gamma \leq 180°$). Its preferred rotation axis is directed between the roll and pitch axes and tipped slightly ventrally, responding to rotations of the opposite sense to those that activate the ipsilateral V1- and V2-cells (Fig. 1D).

The response fields of the V1, V2 and Vx-cells in Fig. 1 plot only the ipsilateral parts of their response fields, including the narrow zone of binocular overlap. Some heterolateral LPTCs including V1 may respond to stimuli presented to the contralateral eye [26, 29], depending on the internal state of the fly [30]. The same holds true for some of the VS-cells including VS6, which responds in a directionally selective manner to stimuli presented to the contralateral eye (Fig. 1I). Though weaker than its ipsilateral motion sensitivity, this contralateral motion sensitivity enhances the cell's response to roll motion. Inspection of the V1, V2 and Vx response fields (Fig. 1B,C,F) suggests that this is most likely to be attributable to excitatory input from the contralateral V2-cell. Along similar lines, simultaneous recordings have already established electrical connections between VS1-3 and the contralateral V1-cell [79], and ipsilateral inhibition of the VS1-cell by the Vx-cell (=Vi) [26]. Simultaneous recordings have also demonstrated electrical coupling of neighbouring VS cells [80]. The putative connectivity diagram in Fig. 1H synthesises these lines of evidence and guides our assumptions on how the signals of the left and right VS-cells are combined to signal specific self-motions.

References

[1] Wehner, R.: 'Matched filters' — neural models of the external world. Journal of Comparative Physiology **161**(4), 511–531 (1987) https://doi.org/10.1007/BF00603659

[2] O'Carroll, D.C., Bidweii, N.J., Laughlin, S.B., Warrant, E.J.: Insect motion detectors matched to visual ecology. Nature **382**(6586), 63–66 (1996) https://doi.org/10.1038/382063a0

[3] Warrant, E.J.: Sensory matched filters. Current Biology **26**(20), 976–980 (2016) https://doi.org/10.1016/j.cub.2016.05.042

[4] Burton, B.G., Laughlin, S.B.: Neural images of pursuit targets in the photoreceptor arrays of male and female houseflies *Musca domestica*. Journal of Experimental Biology **206**(22), 3963–3977 (2003) https://doi.org/10.1242/jeb.00600 https://journals.biologists.com/jeb/article-pdf/206/22/3963/1247489/3963.pdf

[5] Nordström, K., Barnett, P.D., O'Carroll, D.C.: Insect detection of small targets moving in visual clutter. PLOS Biology **4**(3), (2006) https://doi.org/10.1371/journal.pbio.0040054

[6] O'Carroll, D.: Feature-detecting neurons in dragonflies. Nature **362**(6420), 541–543 (1993) https://doi.org/10.1038/362541a0

[7] Geurten, B.R.H., Nordström, K., Sprayberry, J.D.H., Bolzon, D.M., O'Carroll, D.C.: Neural mechanisms underlying target detection in a dragonfly centrifugal neuron. Journal of Experimental Biology **210**(18), 3277–3284 (2007) https://doi.org/10.1242/jeb.008425 https://journals.biologists.com/jeb/article-pdf/210/18/3277/1258750/3277.pdf

[8] Pfeiffer, K., Homberg, U.: Coding of azimuthal directions via time-compensated combination of celestial compass cues. Current Biology **17**(11), 960–965 (2007) https://doi.org/10.1016/j.cub.2007.04.059

[9] Krapp, H., Hengstenberg, R.: Estimation of self-motion by optic flow processing in single visual interneurons. Nature **384**, 463–466 (1996) https://doi.org/10.1038/384463a0

[10] Franz, M.O., Krapp, H.G.: Wide-field, motion-sensitive neurons and matched filters for optic flow fields. Biological Cybernetics **83**(3), 185–197 (2000) https://doi.org/10.1007/s004220000163

[11] Takemura, S.-y., Bharioke, A., Lu, Z., Nern, A., Vitaladevuni, S., Rivlin, P.K., Katz, W.T., Olbris, D.J., Plaza, S.M., Winston, P., Zhao, T., Horne, J.A., Fetter, R.D., Takemura, S., Blazek, K., Chang, L.-A., Ogundeyi, O., Saunders, M.A., Shapiro, V., Sigmund, C., Rubin, G.M., Scheffer, L.K., Meinertzhagen, I.A., Chklovskii, D.B.: A visual motion detection circuit suggested by *Drosophila* connectomics. Nature **500**(7461), 175–181 (2013) https://doi.org/10.1038/nature12450

[12] Maisak, M.S., Haag, J., Ammer, G., Serbe, E., Meier, M., Leonhardt, A., Schilling, T., Bahl, A., Rubin, G.M., Nern, A., Dickson, B.J., Reiff, D.F., Hopp, E., Borst, A.: A directional

tuning map of *Drosophila* elementary motion detectors. Nature **500**(7461), 212–216 (2013) https://doi.org/10.1038/nature12320

[13] Lappalainen, J.K., Tschopp, F.D., Prakhya, S., McGill, M., Nern, A., Shinomiya, K., Takemura, S.-y., Gruntman, E., Macke, J.H., Turaga, S.C.: Connectome-constrained deep mechanistic networks predict neural responses across the fly visual system at single-neuron resolution. bioRxiv (2023) https://doi.org/10.1101/2023.03.11.532232 https://www.biorxiv.org/content/early/2023/03/13/2023.03.11.532232.full.pdf

[14] Taylor, G.K., Krapp, H.G.: Sensory systems and flight stability: What do insects measure and why? In: Casas, J., Simpson, S.J. (eds.) Insect Mechanics and Control. Advances in Insect Physiology, vol. 34, pp. 231–316. Academic Press, ??? (2007). https://doi.org/10.1016/S0065-2806(07)34005-8

[15] Georges, D.: The use of observability and controllability Gramians or functions for optimal sensor and actuator location in finite-dimensional systems. In: Proceedings of 1995 34th IEEE Conference on Decision and Control, vol. 4, pp. 3319–33244 (1995). https://doi.org/10.1109/CDC.1995.478999

[16] Boyacıoğlu, B., Babaei, M., Mamo, A.H., Bergbreiter, S., Daniel, T.L., Morgansen, K.A.: Sensor Placement for Flapping Wing Model Using Stochastic Observability Gramians (2023). https://doi.org/10.48550/arXiv.2310.00127

[17] Wolpert, D.M., Ghahramani, Z., Jordan, M.I.: An internal model for sensorimotor integration. Science **269**(5232), 1880–1882 (1995) https://doi.org/10.1126/science.7569931

[18] Zbikowski, R.: Sensor-rich feedback control: a new paradigm for flight control inspired by insect agility. IEEE Instrumentation and Measurement Magazine **7**(3), 19–26 (2004) https://doi.org/10.1109/MIM.2004.1337909

[19] Krapp, H.G., Taylor, G.K., Humbert, J.S.: The mode-sensing hypothesis: Matching sensors, actuators and flight dynamics, pp. 101–114. Springer, Vienna (2012). https://doi.org/10.1007/978-3-211-99749-9_7

[20] Croon, G.C.H.E., Dupeyroux, J.J.G., De Wagter, C., Chatterjee, A., Olejnik, D.A., Ruffier, F.: Accommodating unobservability to control flight attitude with optic flow. Nature **610**(7932), 485–490 (2022) https://doi.org/10.1038/s41586-022-05182-2

[21] Taylor, G.K., Thomas, A.L.R.: Dynamic flight stability in the desert locust *Schistocerca gregaria*. Journal of Experimental Biology **206**(16), 2803–2829 (2003) https://doi.org/10.1242/jeb.00501

[22] Borst, A., Haag, J., Mauss, A.S.: How fly neurons compute the direction of visual motion. Journal of Comparative Physiology A **206**(2), 109–124 (2020) https://doi.org/10.1007/s00359-019-01375-9

[23] Hausen, K.: Decoding of retinal image flow in insects. Reviews of oculomotor research **5**,

203–235 (1993)

[24] Krapp, H.G., Hengstenberg, B., Hengstenberg, R.: Dendritic structure and receptive-field organization of optic flow processing interneurons in the fly. J. Neurophysiol. **79**, 1902–1917 (1998) https://doi.org/10.1152/jn.1998.79.4.1902

[25] Krapp, H.G., Hengstenberg, R., Egelhaaf, M.: Binocular contributions to optic flow processing in the fly visual system. Journal of Neurophysiology **85**, 724–734 (2001) https://doi.org/10.1152/jn.2001.85.2.724

[26] Krapp, H.: Repräsentation von Eigenbewegungen der Schmeißfliege *Calliphora erythrocephala* in VS-Neuronen des dritten visuellen Neuropils. Dissertation, Eberhard-Karls-Universität, Tübingen (1995)

[27] Strausfeld, N., Seyan, H., Milde, J.: The neck motor system of the fly *Calliphora erythrocephala* — I. Muscles and motor neurons. Journal of Comparative Physiology A **160**(2), 205–224 (1987) https://doi.org/10.1007/BF00609727

[28] Hengstenberg, R.: Gaze control in the blowfly *Calliphora*: a multisensory, two-stage integration process. Seminars in Neuroscience **3**(1), 19–29 (1991) https://doi.org/10.1016/1044-5765(91)90063-T . Sensori-Motor Integration

[29] Karmeier, K., Krapp, H.G., Egelhaaf, M.: Robustness of the tuning of fly visual interneurons to rotatory optic flow. Journal of Neurophysiology **90**(3), 1626–1634 (2003) https://doi.org/10.1152/jn.00234.2003

[30] Longden, K.D., Krapp, H.G.: State-dependent performance of optic-flow processing interneurons. Journal of Neurophysiology **102**(6), 3606–3618 (2009) https://doi.org/10.1152/jn.00395.2009

[31] Kern, R., Hateren, J.H., Egelhaaf, M.: Representation of behaviourally relevant information by blowfly motion-sensitive visual interneurons requires precise compensatory head movements. Journal of Experimental Biology **209**(7), 1251–1260 (2006) https://doi.org/10.1242/jeb.02127

[32] Huston, S.J., Krapp, H.G.: Visuomotor transformation in the fly gaze stabilization system. PLOS Biology **6**(7), 1–11 (2008) https://doi.org/10.1371/journal.pbio.0060173

[33] Longden, K.D., Schützenberger, A., Hardcastle, B.J., Krapp, H.G.: Impact of walking speed and motion adaptation on optokinetic nystagmus-like head movements in the blowfly *Calliphora*. Scientific Reports **12**(1), 11540 (2022) https://doi.org/10.1038/s41598-022-15740-3

[34] Koenderink, J.J., Doorn, A.J.: Facts on optic flow. Biol. Cybern. **56**, 247–254 (1997) https://doi.org/10.1007/BF00365219

[35] Borst, A., Weber, F.: Neural action fields for optic flow based navigation: A simulation study of the fly lobula plate network. PLOS ONE **6**(1), 1–19 (2011) https://doi.org/10.1371/journal.

pone.0016303

[36] Walker, S.M., Thomas, A.L.R., Taylor, G.K.: Operation of the alula as an indicator of gear change in hoverflies. Journal of The Royal Society Interface **9**(71), 1194–1207 (2012) https://doi.org/10.1098/rsif.2011.0617

[37] Faruque, I., Sean Humbert, J.: Dipteran insect flight dynamics. Part 1 Longitudinal motion about hover. Journal of Theoretical Biology **264**(2), 538–552 (2010) https://doi.org/10.1016/j.jtbi.2010.02.018

[38] Faruque, I., Sean Humbert, J.: Dipteran insect flight dynamics. Part 2: Lateral–directional motion about hover. Journal of Theoretical Biology **265**(3), 306–313 (2010) https://doi.org/10.1016/j.jtbi.2010.05.003

[39] Sun, M.: Insect flight dynamics: Stability and control. Rev. Mod. Phys. **86**, 615–646 (2014) https://doi.org/10.1103/RevModPhys.86.615

[40] Walker, S.M., Schwyn, D.A., Mokso, R., Wicklein, M., Müller, T., Doube, M., Stampanoni, M., Krapp, H.G., Taylor, G.K.: In vivo time-resolved microtomography reveals the mechanics of the blowfly flight motor. PLOS Biology **12**(3), 1–12 (2014) https://doi.org/10.1371/journal.pbio.1001823

[41] Nagesh, I., Walker, S., Taylor, G.: Motor output and control input in flapping flight: a compact model of the deforming wing kinematics of manoeuvring hoverflies. Journal of The Royal Society Interface **16** (2019) https://doi.org/10.1098/rsif.2019.0435

[42] Sun, M., Xiong, Y.: Dynamic flight stability of a hovering bumblebee. Journal of Experimental Biology **208**(3), 447–459 (2005) https://doi.org/10.1242/jeb.01407

[43] Zhou, K., Salomon, G., Wu, E.: Balanced realization and model reduction for unstable systems. International Journal of Robust and Nonlinear Control **9**(3), 183–198 (1999) https://doi.org/10.1002/(SICI)1099-1239(199903)9:3<183::AID-RNC399>3.0.CO;2-E

[44] Zbikowski, R.W., Taylor, G.K.: System-theoretic interpretation of the mode sensing hypothesis. Technical Report AFRL-AFOSR-UK-TR-2014-0036, Air Force Research Laboratory (2014)

[45] Gronenberg, W., Strausfeld, N.J.: Premotor descending neurons responding selectively to local visual stimuli in flies. Journal of Comparative Neurology **316**(1), 87–103 (1992) https://doi.org/10.1002/cne.903160108

[46] Wertz, A., Borst, A., Haag, J.: Nonlinear integration of binocular optic flow by DNOVS2, a descending neuron of the fly. Journal of Neuroscience **28**(12), 3131–3140 (2008) https://doi.org/10.1523/JNEUROSCI.5460-07.2008

[47] Wertz, A., Gaub, B., Plett, J., Haag, J., Borst, A.: Robust coding of ego-motion in descending neurons of the fly. Journal of Neuroscience **29**(47), 14993–15000 (2009) https://doi.org/10.

1523/JNEUROSCI.3786-09.2009

[48] Boyacıoğlu, B., Morgansen, K.A.: Bioinspired Observability Analysis Tools for Deterministic Systems with Memory in Flight Applications. https://doi.org/10.2514/6.2021-1679 . https://arc.aiaa.org/doi/abs/10.2514/6.2021-1679

[49] Sterling, P., Laughlin, S.: Principles of Neural Design. The MIT Press, Cambridge, MA (2015). https://doi.org/10.7551/mitpress/9780262028707.001.0001

[50] Krapp, H.G., Hengstenberg, R.: A fast stimulus procedure to determine local receptive field properties of motion-sensitive visual interneurons. Vision Research **37**(2), 225–234 (1997) https://doi.org/10.1016/S0042-6989(96)00114-9

[51] Karmeier, K., R., T., Egelhaaf, M., Krapp, H.G.: Early visual experience and the receptive-field organization of optic flow processing interneurons in the fly motion pathway. Visual Neuroscience **19**(1), 1–8 (2001) https://doi.org/10.1017/s0952523801181010

[52] Franceschini, N.: In: Snyder, A.W., Menzel, R. (eds.) Sampling of the Visual Environment by the Compound Eye of the Fly: Fundamentals and Applications, pp. 98–125. Springer, Berlin, Heidelberg (1975). https://doi.org/10.1007/978-3-642-80934-7_6

[53] Dahmen, H.J., Franz, M.O., Krapp, H.G.: Extracting egomotion from optic flow: limits of accuracy and neural matched filters. In: Zanker, J.M., Zeil, J. (eds.) Motion Vision – Computational, Neural and Ecological Constraints, pp. 143–168. Springer, Berlin, Heidelberg, New York (2001). https://doi.org/10.1007/978-3-642-56550-2_8

[54] Franz, M.O., Chahl, J.S., Krapp, H.G.: Insect-inspired estimation of egomotion. Neural Computation **16**, 2245–2260 (2004) https://doi.org/10.1162/0899766041941899

[55] Humbert, J.S., Murray, R.M., Dickinson, M.H.: Sensorimotor convergence in visual navigation and flight control systems. In: Proceedings of the 16th IFAC World Congress, Praha, Czech Republic (2005). https://doi.org/10.3182/20050703-6-CZ-1902.02003

[56] Humbert, J.S., Hyslop, A.: Bio-inspired visuomotor convergence. IEEE Transactions on Robotics **26**(1), 121–130 (2010) https://doi.org/10.1109/TRO.2009.2033330

[57] Hyslop, A., Humbert, J.S.: Autonomous navigation in three-dimensional urban environments using wide-field integration of optic flow. Journal of Guidance, Control, and Dynamics **33**(1), 147–159 (2010) https://doi.org/10.2514/1.43778

[58] Paul, R., Steiner, A., Gemperlein, R.: Spectral sensitivity of *Calliphora erythrocephala* and other insect species studied with Fourier Interferometric Stimulation (FIS). Journal of Comparative Physiology A **158**(5), 669–680 (1986) https://doi.org/10.1007/BF00603824

[59] Walker, S.M., Thomas, A.L.R., Taylor, G.K.: Deformable wing kinematics in the desert locust: how and why do camber, twist and topography vary through the stroke? Journal of The Royal Society Interface **6**(38), 735–747 (2009) https://doi.org/10.1098/rsif.2008.0435

[60] Badrya, C., Govindarajan, B., Baeder, J.D., Harrington, A., Kroninger, C.M.: Computational and experimental investigation of a flapping-wing micro air vehicle in hover. Journal of Aircraft **56**(4), 1610–1625 (2019) https://doi.org/10.2514/1.C035239

[61] MacFarlane, K., Bush, B., Faruque, I., Humbert, J., Baeder, J.: Quasi-steady and computational aerodynamics applied to hovering drosophila dynamics. In: 29th AIAA Applied Aerodynamic Conference, Honolulu, Hawaii (2011). https://doi.org/10.2514/6.2011-3793

[62] Paganin, D., Mayo, S.C., Gureyev, T.E., Miller, P.R., Wilkins, S.W.: Simultaneous phase and amplitude extraction from a single defocused image of a homogeneous object. J Microsc **206**(Pt 1), 33–40 (2002) https://doi.org/10.1046/j.1365-2818.2002.01010.x

[63] Schindelin, J., Arganda-Carreras, I., Frise, E., Kaynig, V., Longair, M., Pietzsch, T., Preibisch, S., Rueden, C., Saalfeld, S., Schmid, B., Tinevez, J.-Y., White, D.J., Hartenstein, V., Eliceiri, K., Tomancak, P., Cardona, A.: Fiji: an open-source platform for biological-image analysis. Nature Methods **9**(7), 676–682 (2012) https://doi.org/10.1038/nmeth.2019

[64] Doube, M., Kłosowski, M.M., Arganda-Carreras, I., Cordelières, F.P., Dougherty, R.P., Jackson, J.S., Schmid, B., Hutchinson, J.R., Shefelbine, S.J.: BoneJ: Free and extensible bone image analysis in ImageJ. Bone **47**(6), 1076–1079 (2010) https://doi.org/10.1016/j.bone.2010.08.023

[65] Müller, P.C., Weber, H.I.: Analysis and optimization of certain qualities of controllability and observability for linear dynamical systems. Automatica **8**(3), 237–246 (1972) https://doi.org/10.1016/0005-1098(72)90044-1

[66] Dullerud, G.E., Paganini, F.G.: A Course in Robust Control Theory: A Convex Approach. Springer, New York, NY (2000)

[67] Lee, H., Park, Y.: Degree of controllability for linear unstable systems. Journal of Vibration and Control **22**(7), 1928–1934 (2016) https://doi.org/10.1177/1077546314545101

[68] Moore, B.A.: Principal component analysis in linear systems: Controllability, observability, and model reduction. IEEE Transactions on Automatic Control **26**, 17–32 (1981) https://doi.org/10.1109/TAC.1981.1102568

[69] Kenney, C., Hewer, G.: Necessary and sufficient conditions for balancing unstable systems. IEEE Transactions on Automatic Control **32**(2), 157–160 (1987) https://doi.org/10.1109/TAC.1987.1104553

[70] Flinois, T.L.B., Morgans, A.S., Schmid, P.J.: Projection-free approximate balanced truncation of large unstable systems. Phys. Rev. E **92**, 023012 (2015) https://doi.org/10.1103/PhysRevE.92.023012

[71] Hać, A., Liu, L.: Sensor and actuator location in motion control of flexible structures. Journal of Sound and Vibration **167**(2), 239–261 (1993) https://doi.org/10.1006/jsvi.1993.1333

[72] Singh, A., Hahn, J.: Determining optimal sensor locations for state and parameter estimation for stable nonlinear systems. Industrial & Engineering Chemistry Research - IND ENG CHEM RES **44** (2005) https://doi.org/10.1021/ie040212v

[73] Shaker, H.R., Tahavori, M.: Optimal sensor and actuator location for unstable systems. Journal of Vibration and Control **19**(12), 1915–1920 (2013) https://doi.org/10.1177/1077546312451302

[74] Kang, O., Park, Y., Park, Y.S., Suh, M.: New measure representing degree of controllability for disturbance rejection. Journal of Guidance, Control, and Dynamics **32**(5), 1658–1661 (2009) https://doi.org/10.2514/1.43864

[75] Lee, H., Park, Y.: Degree of disturbance rejection capability for linear anti-stable systems. In: 2014 14th International Conference on Control, Automation and Systems (ICCAS 2014), pp. 154–156 (2014). https://doi.org/10.1109/ICCAS.2014.6987977

[76] Marx, B., Koenig, D., Georges, D.: Optimal sensor and actuator location for descriptor systems using generalized Gramians and balanced realizations. In: Proceedings of the 2004 American Control Conference, vol. 3, pp. 2729–27343 (2004). https://doi.org/10.23919/ACC.2004.1383878

[77] Manohar, K., Kutz, J., Brunton, S.: Optimal sensor and actuator selection using balanced model reduction. IEEE Transactions on Automatic Control **67**(4), 2108–2115 (2021) https://doi.org/10.1109/TAC.2021.3082502

[78] Stengel, R.F.: Optimal Control and Estimation. Dover Publications, New York, NY (1994)

[79] Haag, J., Borst, A.: Electrical coupling of lobula plate tangential cells to a heterolateral motion-sensitive neuron in the fly. Journal of Neuroscience **28**(53), 14435–14442 (2008) https://doi.org/10.1523/JNEUROSCI.3603-08.2008

[80] Haag, J., Borst, A.: Neural mechanism underlying complex receptive field properties of motion-sensitive interneurons. Nature Neuroscience **7**(6), 628–634 (2007) https://doi.org/10.1038/nn1245